A versatile nanoreactor for complementary in situ X-ray and electron microscopy studies in catalysis and materials science

Authors

Yakub Fam[a], Thomas L. Sheppard[ab]*, Johannes Becher[a], Dennis Scherhaufer[c], Heinz Lambach[c], Satishkumar Kulkarni[d], Thomas F. Keller[de], Arne Wittstock[f], Felix Wittwer[de], Martin Seyrich[de], Dennis Brueckner[deg], Maik Kahnt[de], Xiaogang Yang[d], Andreas Schropp[d], Andreas Stierle[de], Christian G. Schroer[de] and Jan-Dierk Grunwaldt[ab]

[a]Institute for Chemical Technology and Polymer Chemistry, Karlsruhe Institute of Technology, Engesserstr. 20, Karlsruhe, Baden Württemberg, 76131, Germany

[b]Institute of Catalysis Research and Technology, Karlsruhe Institute of Technology, Hermann-von-Helmholtz Platz 1, Eggenstein-Leopoldshafen, Baden Württemberg, 76344, Germany

[c]Institute for Micro Process Engineering, Karlsruhe Institute of Technology, Hermann-von-Helmholtz Platz 1, Eggenstein-Leopoldshafen, Baden Württemberg, 76344, Germany

[d] Deutsches Elektronen-Synchrotron DESY, Notkestraße 85, Hamburg, 22607, Germany

[e]Department Physik, Universität Hamburg, Luruper Chaussee 149, Hamburg, 22761, Germany

[f]Institute of Applied and Physical Chemistry, University of Bremen, Bremen, 28359, Germany

[g]Faculty of Chemistry and Biochemistry, Ruhr-University Bochum, Universitätsstr. 150, Bochum, 44801, Germany

Correspondence email: thomas.sheppard@kit.edu

Synopsis   A series of nanoreactors have been developed for complementary *in situ* X-ray and electron microscopy. The setup was utilized to monitor thermal annealing processes of porous materials under controlled atmospheres with hard X-ray ptychography.

Abstract   Two *in situ* 'nanoreactors' for high resolution imaging of catalysts have been designed and applied at the hard X-ray nanoprobe endstation at beamline P06 of the PETRA III synchrotron radiation source. The reactors house samples supported on commercial MEMS chips, and were applied for complementary hard X-ray ptychography (23 nm spatial resolution) and transmission electron microscopy, with additional X-ray fluorescence measurements. The reactors allow pressures of 100 kPa and temperatures of up to 1573 K, offering a wide range of conditions relevant for catalysis. Ptychographic tomography was demonstrated at limited tilting angles of at least ±35° within the reactors, and ±65° on the naked sample holders. Two case studies were selected to demonstrate the functionality of the reactors: (i) annealing of hierarchical nanoporous gold up to 923 K under inert He environment; (ii) acquisition of a ptychographic projection series at ±35° of a hierarchically-structured

macroporous zeolite sample under ambient conditions. The reactors are shown to be a flexible and modular platform for *in situ* studies in catalysis and materials science which may be adapted for a range of sample and experiment types, opening new characterization pathways in correlative multimodal *in situ* analysis of functional materials at work. The cells will presently be made available for all interested users of beamline P06 at PETRA III.

Keywords: *in situ*; ptychography; X-ray microscopy; electron microscopy; catalysis.

1. Introduction

In the study of heterogeneous catalysis, derivation of structure-activity relationships is critical to unravel the role of catalysts in chemical processes as well as to improve their performance and stability. Since catalyst structure evolves with the chemical environment present, studies under working conditions (*in situ*) and with simultaneous acquisition of catalytic activity data (*operando*), are of high importance (Topsøe, 2003; Bañares, 2005; Grunwaldt & Clausen, 2002; Weckhuysen, 2002). As catalysts often possess a complex structure, another cornerstone in catalysis research is the collection of spatially-resolved or local structural information. This is often achieved using imaging techniques such as electron or X-ray microscopy or a combination of these (Beale *et al.*, 2010; Frenkel & Van Bokhoven, 2014), especially if information at different length scales is required for a comprehensive understanding of the catalyst (Weckhuysen, 2009; Beale *et al.*, 2010; Grunwaldt *et al.*, 2013). Although superior spatial resolution is normally obtained by electron microscopy (e.g. sub-nm for TEM and 1-50 nm for SEM) and soft X-ray microscopy (De Smit *et al.*, 2008; Thomas & Hernandez-Garrido, 2009) for *in situ* measurements on real catalysts (e.g. powders, pellets), hard X-rays may be regarded as the more suitable probe. Hard X-rays may be applied on up to µm to mm sized samples under more practical working conditions, e.g. 100 kPa or elevated pressures, compared to soft X-ray or electron microscopy (Grunwaldt & Schroer, 2010; Buurmans & Weckhuysen, 2012). At the same time, development of hard X-ray focusing optics is constantly progressing towards smaller beam spot sizes, and spatial resolutions comparable to those of soft x-ray beamlines (Schroer *et al.*, 2017; Seiboth *et al.*, 2017; da Silva *et al.*, 2017; Huang *et al.*, 2015; Yan *et al.*, 2014). In terms of spatial resolution, scanning coherent X-ray diffraction imaging, also known as X-ray ptychography (XRP), has been the main X-ray imaging technique to make a significant breakthrough, i.e. 5 nm for soft X-rays (Shapiro *et al.*, 2014) and 10 nm for hard X-rays (Vila-Comamala *et al.*, 2011; Schropp *et al.*, 2012). Ptychography employs a coherent X-ray beam to scan over the sample, while recording far-field diffraction patterns with a partial overlap between adjacent points in real space. By using iterative phase retrieval algorithms, the overlapping diffraction patterns are then reconstructed into real space images. The use of highly coherent flux and the absence of focusing optics between the sample and detector effectively means that the spatial resolution of ptychography is not limited by the

2

beam spot size, offering excellent potential for high resolution imaging (Guizar-Sicairos *et al.*, 2015; Schropp *et al.*, 2012). However, combining *in situ* measurements with spatially-resolved microscopy at the nanometer scale, including complementary characterization of identical samples by multiple techniques, is a challenging but highly valuable prospect (Weker *et al.*, 2016). While XRP is often used *ex situ* for many applications (Thibault *et al.*, 2008; Hoppe *et al.*, 2013; Piazza *et al.*, 2014; Zhu *et al.*, 2015; Wise *et al.*, 2016; Sala *et al.*, 2018), *in situ* imaging modes, particularly on catalyst materials where accurate control of temperature and gas conditions are essential, have not been widely explored outside of a few pioneering works (Høydalsvik *et al.*, 2014; Van Riessen *et al.*, 2017), including those from our group (Baier, Damsgaard*, et al.*, 2016; Baier, Wittstock*, et al.*, 2016; Baier *et al.*, 2017). Nevertheless, these studies still leave room for improvement in terms of spatial resolution, detection of possible reaction products, and the application of complementary imaging modes (e.g. transmission electron microscopy (TEM), X-ray fluorescence (XRF)), as discussed below. An outlook on the experimental potential of *in situ* X-ray imaging by a range of methods including XRP was recently outlined in literature (Weker *et al.*, 2016). Like other X-ray imaging methods, ptychography can also be applied for tomographic analysis of interior sample structures through a technique known as ptychographic X-ray computed tomography (PXCT) (Dierolf *et al.*, 2010). In catalysis research, PXCT has recently been exploited for example to observe and label pore networks (Li *et al.*, 2019; da Silva *et al.*, 2015), or to identify chemical constituents and their location within global catalyst particles (Ihli *et al.*, 2017; Ihli *et al.*, 2018), while 3D spatial resolutions approaching 23 nm have been demonstrated (Fam *et al.*, 2018). However, since the experimental demands of tomography are significantly more complex than for 2D imaging, performing PXCT *in situ* under precisely controlled gas and temperature conditions undoubtedly constitutes an even greater challenge than for *in situ* ptychography.

One of the first *in situ* XRP studies on catalytic materials was carried out to probe lithium zirconate for CO_2 capture applications. A spatial resolution of 200 nm (Høydalsvik *et al.*, 2014) was achieved, although the experiment was performed in a large gas-filled enclosure, rather than a closed *in situ* cell with controlled internal volume and gas atmosphere. Simultaneous use of *in situ* XRP and XRF nanospectroscopy was later shown to monitor morphological changes and elemental distribution during thermal curing of geopolymers on sub-micrometer length scales, though the experimental apparatus was not fully discussed (Van Riessen *et al.*, 2017). We previously described the design and application of closed *in situ* cells based on micro-electron-mechanical systems (MEMS) chips for XRP of catalyst materials, and studied morphological changes of colloidal gold nanoparticles and nanoporous gold catalysts during thermal annealing under specific gas atmospheres with spatial resolutions down to 20 nm (Baier, Damsgaard*, et al.*, 2016; Baier, Wittstock*, et al.*, 2016). Another application was to study the stability of a $CuO/ZnO/Al_2O_3$-ZSM-5 core-shell material under reducing and oxidizing conditions, obtaining 30 nm spatial resolution (Baier *et al.*, 2017). Notably, the previous

in situ cells could also be used for complementary electron microscopy on identical sample regions. However, the aforementioned setup (Baier, Damsgaard, *et al.*, 2016) possessed some limitations. Apart from a relatively bulky design, high mass (>100 g) and large internal volume, it was not possible to perform complementary XRF imaging or quantify products for *operando* studies, while sample heating was monitored and controlled indirectly via infra-red (IR) thermography. Hence, further improvements are required particularly with regard to sample stability, mechanical vibrations, and experimental control of temperature. Recently, an alternative cell based on MEMS chips was reported for 2D scanning transmission X-ray microscopy (STXM) of Fischer-Tropsch synthesis catalysts under *in situ* conditions (van Ravenhorst *et al.*, 2018). In this case the cell was applied using soft X-rays up to around 800 eV, which necessitates preparation of thin samples in comparison to hard X-ray ptychography.

In this study, we present a series of new and improved *in situ* cells based on MEMS chips for complementary X-ray nanoimaging and spectroscopy measurements of catalysts and other functional materials using synchrotron radiation. The cells were designed to allow high resolution imaging in 2D (2G cell) and tomographic imaging in 3D (3G cell) with limited rotational angles, where 3D volume data may potentially be reconstructed via missing-wedge tomography algorithms without the need to perform a full 180° rotation of the sample. In both cases, the cells can operate under *in situ* conditions, i.e. with controlled temperature up to 1573 K and gas environments up to 100 kPa. The design principles and main features of the 2G and 3G cells are firstly introduced, including discussion on improvement from previous cell designs. Next, experimental case studies are introduced with the newly commissioned cells. 2D XRP was used to monitor thermal sintering and annealing of monolithic nanoporous gold (np-Au) as a bulk catalyst material. A related example of complementary XRP and XRF mapping of 50 nm gold colloids during sintering is shown in the Supporting Information. Furthermore, to demonstrate the possibility of performing 3D PXCT measurements in the cells, a hierarchical micro/macroporous zeolite particle was investigated under a limited rotational angle series of ±35°, with the possibility to extend this to ±65° depending on experimental needs.

2. Experimental

2.1. Design of the *in situ* cells and experimental setup

The *in situ* cells used in this study were designed specifically for use at the hard X-ray nanoprobe endstation at beamline P06 at the PETRA III synchrotron radiation source (Hamburg, DE), although in principle the design is flexible enough for incorporation at similar Nanoprobe beamlines. Two *in situ* cells with specific target functions were commissioned:

- an *in situ* cell for high-resolution *in situ* XRP in 2D, with complementary XRF and/or large angle X-ray diffraction (XRD) mapping, denoted as '2G cell'.

- an *in situ* cell allowing limited-angle 3D *in situ* PXCT in addition to standard 2D XRP, denoted as '3G cell'.

Both cells are based on modular design principles and can be interchangeably integrated into the same setup (Figure 1). For accurate temperature control, a 'Digiheater' temperature controller box and software are used (DENSsolutions, Delft, NL), with printed electrical contacts to interface with the MEMS chip. Mass flow controllers (Bronkhorst High-Tech B.V., Ruurlo, NL) provide accurate control of the gas environment, while a mass spectrometer (Thermostar, Pfeiffer Vacuum GmbH, Aßlar, DE) positioned at the reactor outlet allows for gas analysis. The cell is fixed in a standing position on the beamline stage (Figure 1, top left), which includes lateral piezomotors for nanopositioning and a goniometer for optional center of rotation alignment. Within the cell, there is a 'Wildfire' MEMS chip (DENSsolutions, Delft, NL), on which samples are deposited on the center spiral-shaped sample area (Figure 1, top right). The sample area may be with or without silicon nitride (Si_3N_4) membranes, depending on the experimental requirements and the type of chip used. The operational range of the Wildfire chip is certified at 100 kPa pressure and up to 1373 K with Si_3N_4 membranes, or 1573 K with through-hole chips. The heating zone is indicated by the spiral, but it has been proven to be well-localized within 0.5 mm from the center point. Since the MEMS chips have been commercially utilized for TEM, complementary TEM measurements may readily by performed along with *in situ* XRP and PXCT by simply removing the chip and placing it in an appropriate electron microscopy sample holder.
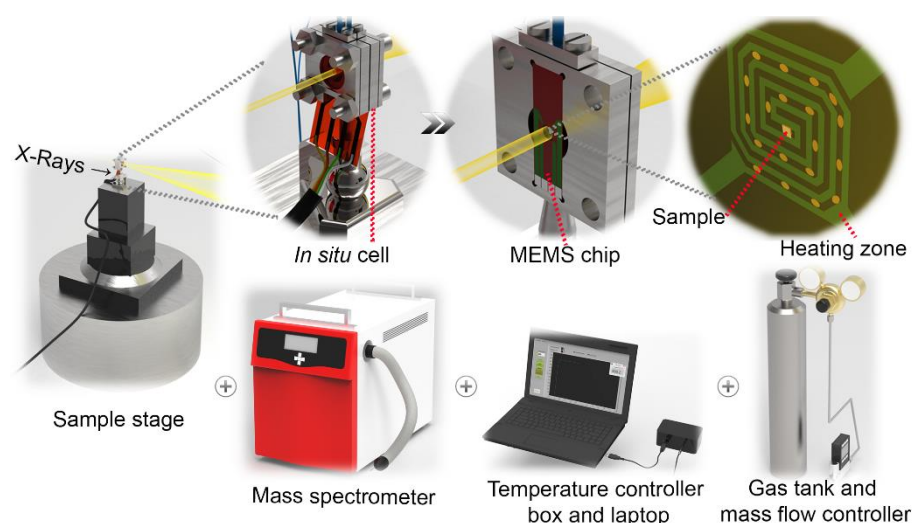

Figure 1 Illustration of the *in situ* setup for 2D and 3D ptychography at the P06 nanoprobe endstation of PETRA III. Top - zooming into the *in situ* cell; bottom - gas and temperature control infrastructure and product analytics.

Both the 2G and 3G cells have the same general configuration, where the top and bottom plates containing the MEMS chip are fixed between O-rings and Kapton films (Figure 2). Small side plates and O-rings provide gas tight sealing of the inlet/outlet gas tubes. Both cells have a similar arrangement for the electrical contact, in the form of a printed circuit (Au on Kapton) which should be positioned on top of the MEMS chip so that the four contact pads on each are well aligned. This electrical contact serves to deliver the current from the temperature controller box (power supply) to the MEMS chip, such that the chip can convert the electrical supply into heat based on the Joule-heating principle. The final similarity between the 2G and 3G cells comes from the small O-ring below the MEMS chip, which also provides gas-tight operating conditions for the cell.
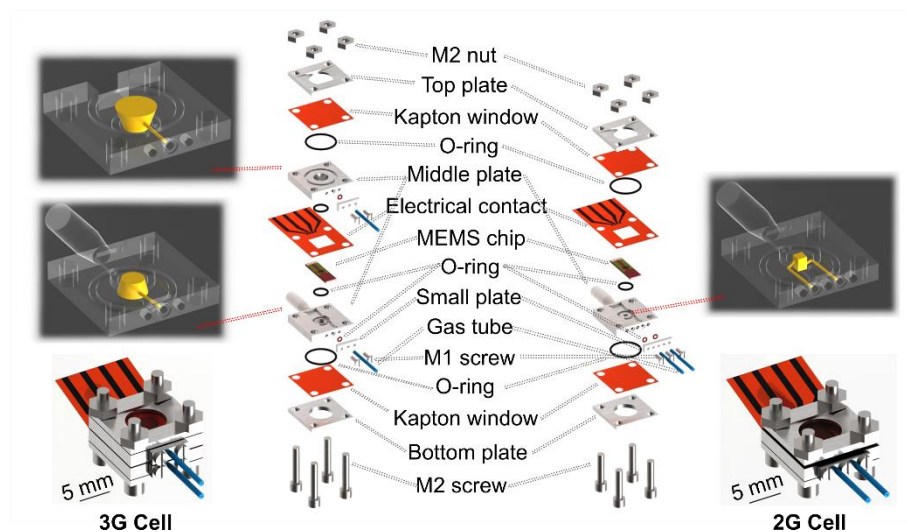

Figure 2 Illustration of disassembled 2G (right) and 3G (left) cell with their internal gas-flow volumes (highlighted above). The fully assembled setups are shown below.

Beyond these aspects, there are some noticeable differences in design and function between the 2G and 3G cells. The use of one middle plate for 2G along with Si_3N_4 membrane MEMS chips, but two middle plates for 3G with through-hole MEMS chips, directly influences the internal volume of the cells. The 2G cell has around 2.6 µl internal volume and the 3G around 24.5 µl, thus the word "nanoreactor" is used in this work due to internal volumes approaching 1 µl. Fluid flow simulations were performed to demonstrate the gas flow principle in each cell as shown in Figure 3 (description in Supporting Information S1). For 2G, the gas flows into the single middle plate, across the underside of the sample deposited on the back of MEMS-chip, and then out once again from the same plate (Figure 3). Meanwhile for 3G, the gas flows from the bottom middle plate, directly through the sample deposited on the through-hole MEMS chip, and finally to the outlet port of the top middle

plate (Figure 3). Sample drift as a result of gas flow/pressure in the cell is expected to be negligible, due to low Reynold's number of 9, while the MEMS chips are typically used for environmental transmission electron microscopy (ETEM) which is considerably more sensitive to sample drift due to the highly focused electron beam. Regarding cell mounting, the 2G cell has to be placed directly perpendicular to the incident X-ray beam, while the 3G cell allows tilting of ±35° around the center of rotation with respect to the beam (or ±65° for the naked MEMS chip). The intention is that all kind of samples can be used for 2G, including colloids, size-selected clusters or unsupported samples which require a membrane for stability. However, imaging studies are then limited to 2D XRP. On the other hand, the 3G cell with through-hole chips can exploit both 2D XRP and limited-angle PXCT, but this is restricted to pre-shaped samples which are then fixed to the chip through focused ion beam (FIB) manipulation or similar techniques. The general intention is to provide maximum flexibility to users of the hard X-ray nanoprobe endstation of beamline P06, who often have diverse sample requirements and structural features of interest.
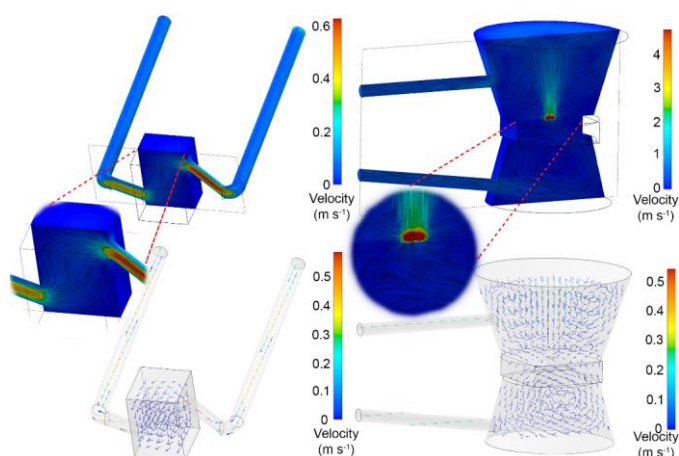

Figure 3 Internal gas-flow volume and simulation of 2G cell (left) and 3G cell (right).

2.2. Sample preparation and mounting

In terms of sample dimensions, in the plane of the MEMS chip (x, y axis) can reach up to 0.5 x 0.5 mm^2, equivalent to the heating area. However, the maximum sample thickness (z axis, vertical height above the heating area) has not been definitively shown. While the cell can physically accommodate samples with several hundred microns thickness, to obtain uniform heating the sample should probably not extend more than several tens of microns above the heating area. Ensuring uniform heating will also greatly depend on the sample used, with respect to thermal conductivity. Since technical catalysts often possess dimensions up to mm scale, an accurate *in situ* experiment will typically involve a degree of sample preparation. This may for example be through selection of small

grains of a catalyst sample through abrasion, grinding or sieving from larger bodies, analogous to TEM sample preparation. Alternatively, for extracting sub-volumes of shaped or hierarchically structured materials where preservation of the structure is essential, the use of FIB, He-ion microscopes, or similar instruments may be required. This is necessary both to shape the sample and to deposit it correctly on the MEMS chips. Preparation of samples representative of the global material of interest should therefore be carefully considered. However, it should be noted that the range of typical sample dimensions permitted still greatly exceeds those feasible using TEM, due to relatively greater attenuation of electrons compared to hard X-rays.

Two sample types were used to demonstrate the use of the cells; (i) monolithic np-Au, (ii) hierarchical zeolite with intracrystalline macropores. Pure np-Au samples were prepared by dealloying of an Ag-Au alloy (i.e., 70 at% Ag and 30 at% Au) in nitric acid (65 wt%) as previously published (Lackmann *et al.*, 2018). The sample was placed on an SEM sample holder stub (Figure S1), introduced to the FIB setup, then cut and shaped with a Ga^+ ion beam into a wedge (Figure S2, S3). The thicker part (1 µm) was used for *in situ* XRP and thinner part (0.2 µm) for *ex situ* TEM. The wedge was extracted with the micromanipulator and placed across the window of a through-hole Wildfire chip (Figure S4), before being fixed by Pt glue at each corner. The as-prepared np-Au wedge sample is shown in Figure 4c-4d. Macroporous zeolites were synthesized by a templating method using silica and alumina precursors, followed by steam assisted crystallization to form macropores within the crystals, as described in previous publications (Machoke *et al.*, 2015; Schwieger *et al.*, 2016). The zeolite powder consisting of 2-4 µm crystals was introduced to the FIB setup, a suitable grain selected and placed across the window of a through-hole Wildfire chip, before being fixed with Pt-glue on one side. The as-prepared zeolite sample is shown in Figure 4a-4b. Sample preparation by FIB was performed at DESY NanoLab (Stierle *et al.*, 2016). A detailed description of the different sample preparation steps is illustrated in the Supporting Information (Figure S1-S4). TEM, energy dispersive X-ray spectroscopy (EDX), and selected area electron diffraction (SAED) measurement were performed using a Wildfire sample holder (DENSsolutions, Delft, NL), on a Titan 80-300 (FEI) microscope operated at an acceleration voltage of 300 kV in STEM and TEM mode, at the Institute of Nanotechnology (INT) at Karlsruhe Institute of Technology.
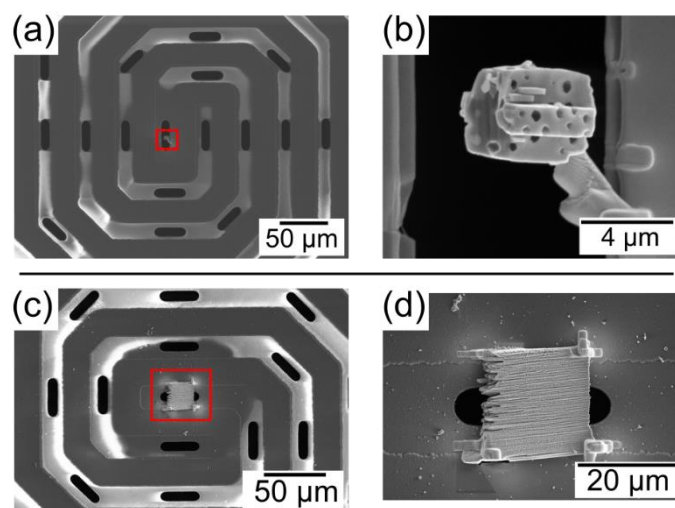
Figure 4 SEM images obtained during FIB preparation on Wildfire chips at DESY NanoLab: (a) micro/macroporous zeolite crystal and (b) zoom in of the highlighted area; (c) monolithic np-Au wedge and (d) zoom in of the highlighted area.

2.3. *In situ* synchrotron X-ray imaging studies

All experiments were performed at the nanofocus endstation of beamline P06 at the PETRA III synchrotron radiation source (Hamburg, Germany) using the measurement parameters shown in Table 1. All XRP measurements were performed using an EIGER X 4M detector (DECTRIS Ltd, Switzerland) with 75 x 75 µm^2 pixel size and 2070 x 2167 pixels. Measurement of np-Au and macroporous zeolites were performed during two separate beamtimes. For measuring the whole sample of np-Au, a field of view of 20 x 20 µm^2 was used with 14 min scantime per image. For the smaller 5 x 5 µm^2 field of view indicated in Table 1, a region of interest was selected from the center of the sample wedge. The different choice of exposure time for the np-Au and zeolite samples is due to measurement in focal position with high scattering (pure Au sample), compared to measuring out of focus on a relatively weaker scattering sample (zeolite, Si/Al).

For *in situ* measurement of the np-Au sample, pure helium with a specific inlet flow of 1 ml/min adjusted by a mass flow controller was used to maintain a controlled atmosphere during *in situ* annealing treatment. The temperature was controlled via Joule heating and monitored using customized Labview software. Specific temperature conditions applied during imaging are indicated next to the relevant figures in the results section. The outlet flow from the cell was analyzed online using a Thermostar quadrupole mass spectrometer (Pfeiffer Vacuum GmbH, Aßlar, DE) to confirm the desired atmospheric composition was present during *in situ* experiments. In this case, He and residual O_2 (m/z = 4, 32) were monitored for the inert atmosphere. For measurement of the hierarchical zeolite by limited angle tomography, the sample on a Wildfire chip was placed within the 3G cell and aligned to the center of rotation with respect to the beam. 2D ptychographic projections

9

were recorded across an angular range of approximately ±35° in 1.4° steps, leading to a total of 51 projections. The zeolite was scanned in a raster grid with each scan point randomly offset in both scanning directions by up to 50% of the step size, known as grid jitter mode.

Table 1   Experimental parameters during XRP studies at P06 beamline of PETRA III.

Sample Type	np-Au	np-Au	Zeolite
Energy (keV)	9.0	9.0	9.0
Sample to detector distance (mm)	2310	2310	3470
Sample focus distance (mm)	in focus	in focus	0.6
Field of view (μm^2)	5 x 5	20 x 20	4 x 4
Exposure time (ms)	10	5	500
Scantime per image (min)	3-4	4-5	5-6
Beam size on the sample (nm)	60	60	2000[b]
No. scanpoints	125 x 125 = 15625	200 x 200 = 40000	12 x 12 = 144
Scan step size (nm)	40	100	333
Scan type and dimensions (μm^2)	Continuous, 5 x 5	Continuous, 20 x 20	Grid jitter mode, 4 x 4
Optics	FZP[a], 125 µm aperture, 70 nm outermost zone width, 30 µm pinhole, 60 µm central stop, focal length 63.5 mm, beam divergence 1 mrad		

[a]Fresnel zone plates, [b]out of focus

2.4. Data processing

The algorithm used for ptychographic reconstruction was based on the (e)PIE algorithm (Maiden & Rodenburg, 2009). Cropping the diffraction patterns to 256×256 pixels led to a pixel size of 8.2 nm (for np-Au), and 8.5 nm (for zeolite) in the reconstructed images. To estimate the spatial resolution, a Fourier ring correlation (FRC) analysis (Van Heel & Schatz, 2005) was performed (Figure S6-S8). Correlation was always performed on 2D projections (ring correlation), as opposed to 3D volumes (shell correlation). As a common procedure, two individual successive scans of an identical sample area were reconstructed and compared. First the images were cropped to exclude the edges of the field

of view, phase wedges were removed and the images were aligned on a sub-pixel level using the "scipy" Python package (Guizar-Sicairos *et al.*, 2008). Before correlating the phase reconstruction, a Kaiser-Bessel window function with a size equal to 1 was applied to the images, in order to reduce artifacts caused by erroneous high frequencies resulting from the edges of the limited field of view of the reconstructions.

Tomography reconstruction of the ptychographic projection series for the hierarchical zeolite sample was performed as follows. The 51 reconstructed phase projections were first cropped to only include the sample area present within the window of the MEMS chip. Secondly phase wedges and offsets were removed from the projections, using the regions right next to the sample as the zero-reference point. The third step was to align all projections to each other in the vertical direction (along the rotation axis) by correlating the derivative of their vertical profiles (Guizar-Sicairos *et al.*, 2011). Step four was the horizontal alignment (in the tomographic plane) by aligning the horizontal center of mass of all projections. This placed the rotation axis into the center of mass of the particle. The obtained sinogram was reconstructed using multiple tomography algorithms, including: (i) simultaneous iterative reconstruction technique (SIRT) from the "TomoJ" package (Messaoudii *et al.*, 2007), as implemented in FIJI software (Schindelin *et al.*, 2012), (ii) simultaneous algebraic reconstruction technique (SART) (Andersen & Kak, 1984), as part of the Python package "scikit-image" (van der Walt *et al.*, 2014), (iii) maximum-likelihood expectation maximization (MLEM) algorithm using in-house code based on the literature (Bruyant, 2002), (iv) an in-house deep learning code in development at beamline P06 of PETRA III for analysis of limited angle tomography data (in preparation).

3. Results

3.1. Design process for the 2G and 3G *in situ* cells

The design of the 2G and 3G cells was directly inspired by the first generation *in situ* XRP cell developed by our group, denoted here as the 1G cell (Baier, Damsgaard*, et al.*, 2016). Development of the next generation cells was driven by several significant practical limitations of our own 1G cell and those previously described in the literature, which are summarized in the following section.

One of the first applications of in situ 2D XRP was to monitor CO_2 capture on Li_2ZrO_3 materials, which was performed in a plexiglass sample enclosure. However, such an open sample environment is considerably different in volume to a closed reactor or cell. Both exclusion of ambient air and maintaining a defined gaseous environment such as CO_2 are therefore challenging tasks, particularly if hazardous gases are required (Høydalsvik *et al.*, 2014). Later experiments used a scanning chip calorimeter to visualize thermal annealing processes in organic photovoltaic layers in combination

11

with 2D XRP (Patil *et al.*, 2016; Van den Brande *et al.*, 2017). Although showing an excellent control over annealing temperatures with this setup, the same issue with controlling the gas environment is present and such a system is not optimal for heterogeneous catalysis studies with defined reaction conditions. A separate study used *in situ* XRP to observe the microstructure changes of geopolymers during thermal curing processes (Van Riessen *et al.*, 2017), but unfortunately the setup and sample environment were not detailed, while it appears that the samples were heated in an open atmosphere. Recently an alternative cell design based on MEMS chips was reported with some similarities to that of the current work (van Ravenhorst *et al.*, 2018). The authors demonstrated the application of STXM on a Fischer-Tropsch catalyst particle with 50 nm spatial resolution, specifically by performing spectroscopic measurements with soft X-rays around the Co L_{2-3}, Ti L_{2-3} and C K edges in absorption contrast mode. However, soft X-rays generally necessitate more invasive preparation of thin samples in comparison to hard X-rays Furthermore, the geometry of the cell (e.g. beamline mounting, window exit angle) may not permit complementary measurements such as nanofluorescence or nanodiffraction, limiting the experimental flexibility of the system compared to the 2G/3G cell setup described here. Furthermore, the highly focused 50 nm beam for STXM requires strict minimisation of sample drift and mechanical vibrations. On the other hand, ptychography can offer superior spatial resolution independent of the beam spot size, allowing samples to be scanned in or out of the beam focal point (Schropp *et al.*, 2012; Guizar-Sicairos *et al.*, 2015; Hönig *et al.*, 2011), as shown in the current work. Measuring out of focus can generally result in more rapid scan times over larger sample volumes for ptychography while relaxing the limitations of sample drift over time, compared to STXM which requires a highly focused beam to obtain high spatial resolution. Furthermore, XRP offers the possibility to obtain complementary spectroscopic information through resonant XRP imaging (Hoppe *et al.*, 2013; Ihli *et al.*, 2018), or to identify and locate sample constituents by converting the observed phase shift to yield electron density maps of the sample (Diaz *et al.*, 2012). Unlike the 3G cell, the geometry of the alternative MEMS chip design is also not suitable for 3D imaging either in electron microscopy or potentially with PXCT, although complementary TEM studies would be feasible.

Our previous work with the 1G cell was able to demonstrate complementary TEM and XRM, a contained gas environment and a wide range of applicable temperatures with indirect heating provided by a variable voltage power supply and an IR thermography camera. A point-by-point comparison of the 1G cell with the 2G and 3G cells presented in this work follows. The 2G and 3G cells described here have been improved with respect to many of the criteria mentioned above, particularly with respect to the 1G cell developed by our group. Firstly, they both exhibit significantly smaller internal gas flow volumes (volume ratio of 1G:2G:3G = 500:2.6:24.5 µl = 192:1:9). This is an important factor in determining the sample sizes necessary for *operando* studies, where the smaller the internal volumes, the more freedom available to use smaller sample sizes while being able to reliably detect

dilute products. On the other hand, where relatively larger sample volumes are used, reactant conversion may be high enough to allow quantitative product analysis in addition to imaging. The sample size is therefore an important criterion both for the purpose of mass spectrometry characterization of the gas stream outlet, but is also relevant if complementary TEM studies are required. Preparation of relatively large or thick samples by FIB is both time intensive and may result in attenuation of the electron beam and poor resolution. The ability to effectively image either thick samples with X-ray imaging, or thin samples with electron and X-ray imaging adds a layer of flexibility to the possible uses of the setup (see np-Au wedge study below). In addition, the low internal cell volume actually leads to a smaller physical profile of the cell, which generally decreases the total weight of the setup. This is crucial to ensure accurate and error-free nano-precise positioning of the setup by the beamline sample stage motors. The 2G and 3G cells therefore come with a significant decrease in size and mass compared to the 1G cell and other cells reported earlier.

Another advantage of the current cells is the additional characterization capabilities on offer. Spectroscopic XRF analysis is possible in addition to XRP, which is extremely useful to map elemental distribution within the probed material. Although methods are available to accurately determine elemental speciation using XRP (e.g. resonant imaging around an elemental absorption edge (Hoppe *et al.*, 2013)), XRP does not always guarantee chemical contrast in the sample of interest. For ptychography beamlines optimised in the use of nanofocusing optics, such as P06 at PETRA III, the acquisition of highly spatially-resolved local fluorescence data is a natural advantage due to the small beam size. Provided the incident energy is above the absorption edge of interest, XRF mapping is complementary to XRP. Such measurements were not possible with the 1G cell due to the bulky cell body, which did not allow detector positioning at an appropriate angle to detect measurable fluorescence counts. At the moment XRF must be performed following slight rotation (25-35°) of the cells to face the detector, which can be positioned around 110° relative to the incident X-ray rather than the optimal angle of 90°. This also means that simultaneous XRF and XRP are not optimal, although they can be sequentially acquired on congruent sample fields of view with little delay between measurements. However, the necessary beam conditions for simultaneous XRF and XRP measurement modes are not always complementary in any case. Furthermore, the 3G cell has been designed for PXCT with limited angles, similar to the missing wedge principle commonly employed in electron tomography. This allows for large angle XRD up to a 2θ range of around 70°. The 1G cell was on the contrary strictly limited to 2D XRP.

The temperature control system is one of the most significant improvement over the original 1G setup. The 2G and 3G cells exhibit a direct and fast response to programmed temperature input due to the use of MEMS chips with 4-point resistivity measurement, allowing temperature readout and control in a feedback loop (see Supporting Information Figure S5). This capability has also been widely used in the *in situ* Wildfire series TEM sample holders (Ren *et al.*, 2018; Gocyla *et al.*, 2018).

Furthermore, the specific resistivity of each chip under ambient conditions is calibrated during manufacture, improving the accuracy of all temperature-controlled experiments. With the 1G cell, no temperature feedback was used, necessitating a variable voltage power supply system and indirect temperature measurement with an IR camera, whose temperature readout and control is significantly less effective. This is partly due to the delay in recording the temperature from the camera and manually adjusting the power supply to obtain the desired condition. However, the indirect control mechanism also leaves the system vulnerable to unexpected changes in temperature, e.g. from changing gas conditions and therefore specific heat capacity of the local environment, or from thermal variation due to chemical reactions taking place on the chip. In summary, the cells offer significant current and potential improvements over similar setups previously described in literature:

- compatibility with a range of sample types, including colloids, metal nanoparticles, bulk materials and single catalyst grains;

- maintenance of a closed cell with easily controllable gas environment, allowing the application of oxidative, reductive or hazardous gases in a safe manner;

- small ratio of internal cell volume to sample volume, permitting high contact time between samples and reactant gases, and potentially facilitating the detection of gaseous products during X-ray imaging when large enough samples are present (*operando* imaging);

- low mass of the setup, mitigating vibrational instabilities and positioning errors when using nanoprecise sample stage motors, thereby leading to improved spatial resolution;

- capability to perform several complementary measurements (possibly simultaneously), including XRF, large angle XRD (nanospectroscopy / nanodiffraction);

- capability to perform complementary electron microscopy and ptychography on identical samples, including *in situ* electron microscopy with an appropriate sample holder;

- capability to perform 3D imaging by acquiring 2D projections at limited rotational angles;

- direct and accurate resistive heating, which may be easily programmed, monitored and precisely controlled via a feedback mechanism (± 0.01 K in Figure S5) under specific desired gas atmospheres (e.g. inert He, O_2, H_2, reactive gases);

3.2. Annealing of np-Au series in controlled gas environment using the 2G cell

The annealing of hierarchically-structured np-Au was chosen as a case study to demonstrate the capabilities of the fully commissioned in situ cells (Figure 2) and related infrastructure (Figure 1). Nanoporous gold is an ideal sample for XRP due to high phase contrast and large difference in electron density between the substrate and background air (Fam *et al.*, 2018). Moreover, np-Au has a

hierarchical structure of sponge-like 3D network, where its pores and ligaments form a macroscopic material spanning from nanometer to millimeter scales (Wichmann *et al.*, 2013; Bagge-Hansen *et al.*, 2014; Shi *et al.*, 2014; Shi *et al.*, 2016; Shi *et al.*, 2017). This makes np-Au an excellent benchmark for evaluating the highest resolution achievable under *in situ* conditions (Larsson *et al.*, 2019). Experiments were performed at elevated temperature up to 923 K while flowing He (1 ml/min) through the cell. A large 20 x 20 µm² overview scan of the np-Au wedge was recorded before and after heat treatment. For the high resolution *in situ* imaging series, a smaller 5 x 5 µm² field of view was selected from the center of the sample wedge. XRP reconstructions of the overview scan and selected *in situ* images are shown in Figure 5, with an estimated spatial resolution of 23 nm (Figure S7). The through-hole window of the MEMS chip can be observed as a lighter rounded rectangle shape in the middle of Figure 5a-b. Notably for hard X-ray imaging it is not strictly necessary to place the sample directly over such a window, although this will reduce background scattering. For potential TEM measurements on the other hand, the sample must be placed over such a window.
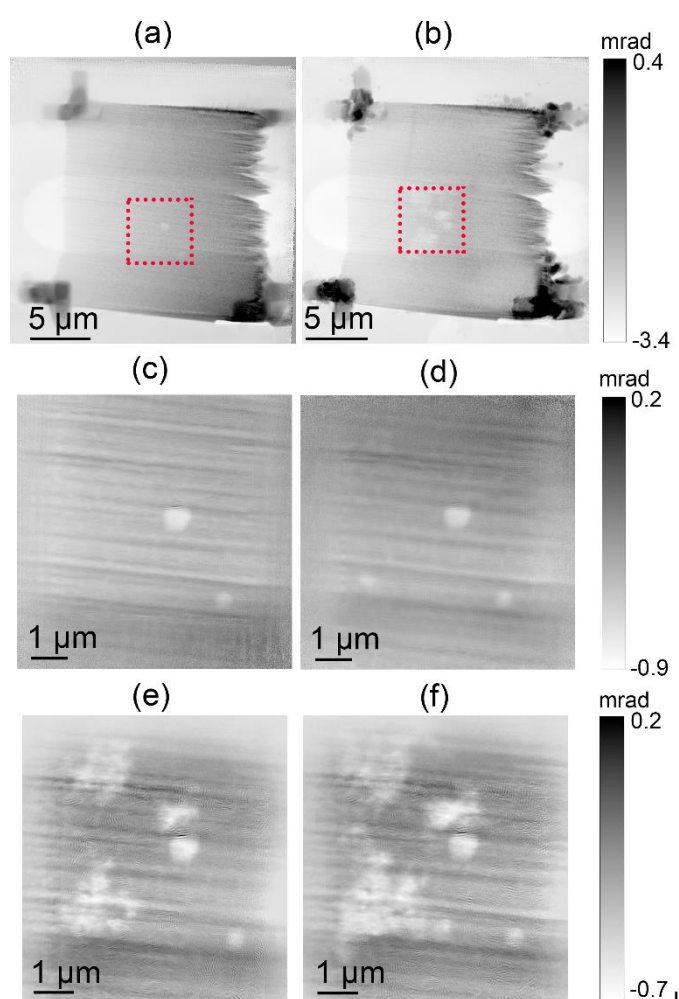
Figure 5 Ptychography images from thermal annealing of np-Au under He environment. Overview scans: (a) before and (b) after thermal annealing. Highlighted area in (a-b) shown: (c) at 293 K, (d)

923 K after 0 min, (e) 923 K after 15 min, (f) 923 K after 30 min. Darker intensity in phase maps indicates areas rich in Au, while brighter voids indicate annealing and absence of Au ligaments. Pt glue from FIB is visible as intense features in the corners of (a-b).

The sample was thermally stable under inert gas atmosphere up to 923 K, after which the coarsening process was strongly visible. The temperature was kept constant at 923 K and sequential 2D XRP images were acquired to illustrate the progression of the coarsening process. The high accuracy of the temperature control system can be seen in the experimental readout plot in the supporting information (Figure S5). Coarsening was observed as large-scale annealing of fine gold ligaments (which were previously at or below the resolution limit), to form larger ligaments and leaving behind irregular shaped voids of lower electron density, therefore lower local concentration of Au. Individual ligaments are faintly visible around the voids in Figure 5e-f. In comparison with previous experiments on np-Au, the coarsening process was studied by both *in situ* TEM and *in situ* ptychography, with the onset of coarsening found to be at 523-573 K in 100 kPa of synthetic air (20% O_2/N_2), 573 K in 320 Pa of pure O_2, and 973 K in vacuum. (Baier, Damsgaard, *et al.*, 2016; Baier, Wittstock, *et al.*, 2016). It was previously concluded that both the atmosphere composition and the pressure affect material stability. An oxygen containing atmosphere at any pressure may reasonably be expected to interact more strongly with the Au surface that inert He, therefore the onset of coarsening observed here at 923 K lies somewhere between the values observed in synthetic air or pure oxygen, and vacuum conditions. This additionally proves the maintenance of an inert environment inside the cell. A notable improvement over previous measurements is that these were carried out at 100 K intervals (TEM studies) and 25-30 K intervals (*in situ* XRP), whereas here it was possible to use consecutive temperature steps of 10 K, leading to greater precision in determining the coarsening onset temperature. Comparing the first and last overview image in Figure 5a-b, it should be noted that the Pt glue fixed on the corner of the sample for stability via FIB partly disintegrated. For future studies the deposition of more temperature stable materials, e.g. tungsten, may be an advantage. Another important point to consider in this case is the unavoidable thermal drift caused by expansion of the MEMS chip viewing area, which prompts users either to find a 'natural' marker for determining the extent of drift from the area of interest, or to make a synthetic marker, e.g. deposition of Pt ring, via FIB prior to XRP measurements. In this experiment, the edge of the MEMS chip window was used as a natural marker. Also notable is how the coarsening process appeared to be more intense precisely in the area scanned continually during the temperature series. This aggravated coarsening behavior is suggested to be influenced by beam effects, since the area outside the field of view was less affected.

To demonstrate the possibility for complementary measurements on a single sample, TEM was conducted on the thin part of the np-Au wedge before and after *in situ* XRP as shown in Figure 6. The structural difference is noticeable particularly between Figure 6b-d, where the np-Au ligaments appear

more consolidated as expected following thermal annealing at 923 K (Baier, Damsgaard, *et al.*, 2016; Baier, Wittstock, *et al.*, 2016). In addition, some minor contamination was observed at the border of the ligaments (Figure 6b), which was characterised as containing Si and Pt using EDX analysis (see Supporting Information Figure S12, EDX quantification in Table S1). Such contamination could originate from the Si_3N_4 layer present on the MEMS chips or the Si chip body, which may have been deposited during the process of attaching the sample wedge to the Wildfire chip by FIB. This would also explain the source of Pt contamination, during gluing of the wedge to the MEMS chip. The Si layer was still detected even after thermal treatment (Figure 6d) although it became significantly thinner probably due to the influence of high temperature. While such contamination is unfortunate, it is also a common feature of FIB preparation and is difficult to exclude, however it is not expected that the complete sample wedge was affected particularly for XRP measurements, where the sample thickness in the region of interest was estimated as 600 nm. The composition of the np-Au sample was also confirmed as metallic gold by examining the Au lattice spacing by high resolution TEM (d = 0.236 nm, [1 1 1] plane of Au crystal (PDF 99-0056)) and by SAED (d = 0.234 nm) (see Supporting Information Figure S13-S14). These measurements prove the capability of the setup to allow detailed characterisation of identical samples by X-ray and electron microscopy, giving access to multiple sample length scales and spatial resolutions down to sub-nanometer level.
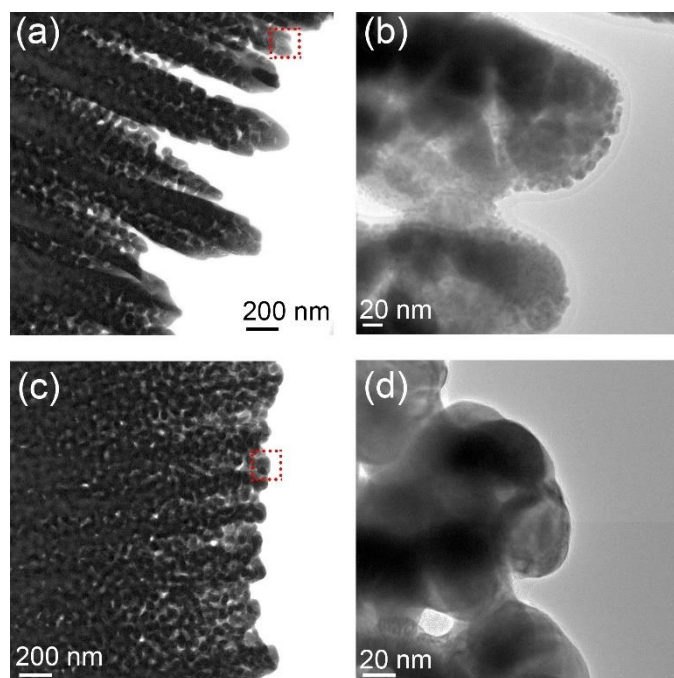
Figure 6 TEM images of np-Au: (a) before *in situ* thermal annealing and (b) zoom in on the highlighted area; (c) after *in situ* thermal annealing at 923 K and (d) zoom in on the highlighted area.

3.3. Limited rotational angle 3D ptychography of hierarchical macroporous zeolite using the 3G cell

The 3G cell used in this case study matches all the experimental capabilities of the 2G cell described previously. However, the 3G cell was designed to furthermore permit *in situ* imaging under a range of tilting angles, therefore unlocking *in situ* PXCT in a closed cell as a viable characterization technique. To demonstrate the potential of the 3G cell to perform PXCT firstly under ex situ conditions, a ptychographic projection series at various tilting angles was acquired from a single crystal of hierarchically porous zeolite. Consisting of 2-4 µm crystals enclosing micropores (< 2nm) along with interior voids of several hundred nm, the macroporous zeolite therefore functions as a good test sample for 3D imaging, with strongly identifiable interior features (Machoke *et al.*, 2015; Schwieger *et al.*, 2016; Przybilla *et al.*, 2018). It should be noted that the zeolite micropores present (<2 nm) are challenging to observe except potentially with high resolution electron microscopy, which was not performed on the specific sample used here. Tomographic PXCT measurements were performed at ambient temperature and in He gas environment with the sample placed in the fully assembled 3G cell. Figure 7d shows the ptychographic image taken at 0° tilting angle, i.e. with the cell in its normal position perpendicular to the incident beam. The macroporous structure of the zeolite can clearly be observed as a series of spherical voids within the catalyst grain. The permitted angular range was eventually found to be approximately ±35° with the cell fully assembled, as indicated by the image series shown in Figure 7. Beyond these, the X-ray beam was partially blocked by the cell body, greatly compromising the quality of the reconstructed images. Notably, by removing the chip from the cell body, rotational angles of ±65° could be reached. While images were acquired at ambient temperature, this was not due to limited functionality of the cell but rather due to high thermal stability of the zeolite material and the lack of any obvious thermal annealing process like for np-Au. The zeolite sample served primarily as a test object, but was measured within the assembled 3G cell, which is known to have identical control over temperature and gas conditions as the 2G cell presented earlier. The zeolite serves therefore as a good proof-of-concept study for combining PXCT and *in situ* measurements on other systems in the future, such as *in situ* drying, annealing or chemical reactions. The acquisition of partial data due to geometric limitations draws comparison to both electron tomography where missing wedges are unavoidable (Arslan *et al.*, 2006), and laminography where the sample is positioned almost horizontal in the plane of the X-ray beam and rotated non-perpendicularly with respect to the beam (Odstrcil *et al.*, 2018). In both cases however, *in situ* implementation of such methods can be challenging under a controlled temperature and gas environment, while the geometry of the 3G cell has more in common with electron tomography than laminography.
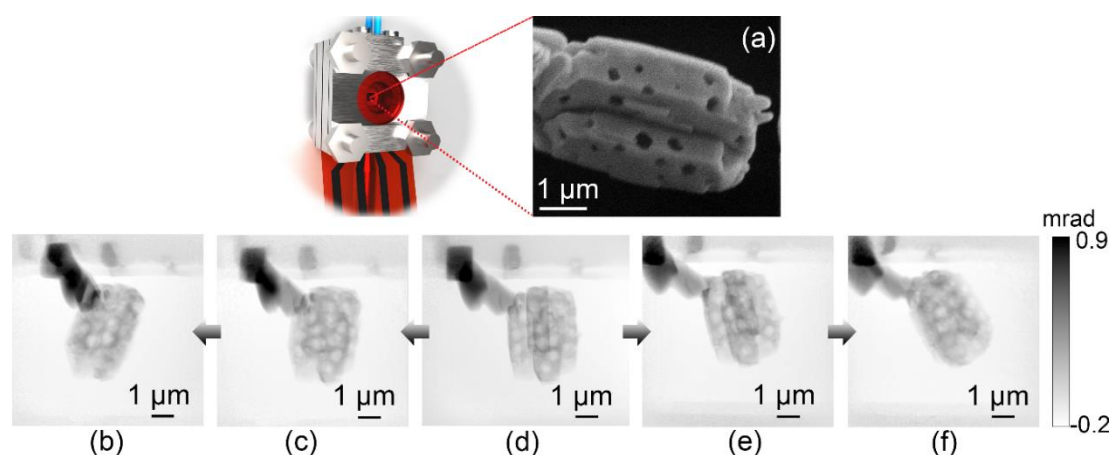
Figure 7 Tilting angle tests using micro/macroporous zeolite as a case study: (a) illustration of the 3G cell with corresponding SEM image of the zeolite crystal on a MEMS chip, and ptychography images of the specimen at tilting angles with respect to the incident beam: (b) 35°, (c) 15°, (d) 0°, (e) -15°, (f) -35°. Dark spots in phase maps indicate areas rich in Si/Al. Pt-glue is visible as the dark region in the upper left of each image.

Despite the limited rotational range and relatively low number of projections acquired leading to a large missing wedge, it was possible to perform rudimentary tomographic reconstruction of the data. The results of several reconstruction methods are shown in Figure 8. As expected from the suboptimal data acquisition parameters and the missing wedge, typical reconstruction methods such as SART, SIRT and MLEM produce significant artefacts such as 'cats eye' broadening of the roughly spherical zeolite pores, and significant blurring of edge features (Kupsch *et al.*, 2016). In an attempt to improve the reconstruction quality and mitigate missing wedge effects, a deep learning reconstruction technique currently in development at beamline P06 (DESY) for handling such data was employed. As shown in Figure 8a, this significantly improved the appearance of the zeolite data, where the pores, which are known to be close to spherical (Figure 7), also appear as spherical pores. While the application of this technique is still at an early stage, there are in any case several opportunities for improving the data acquisition range and therefore the quality of the reconstructed data which can be obtained by any of the above reconstruction techniques. Firstly, in the case that a contained sample environment is not necessary throughout an entire experiment, the sample can readily be treated under certain conditions of temperature or gas, then simply removed from the cell at regular intervals to perform tomography scans. This procedure could be repeated to obtain an image series during thermal treatment covering ±65°, which nearly doubles the measurable angular range and more than halves the size of the missing wedge compared to a rotational series inside the cell. Notably, an angular range of ±65° is similar to the missing wedge data routinely recorded using electron tomography (Zečević *et al.*, 2013; Midgley & Dunin-Borkowski, 2009). Secondly, if maintaining an *in situ* environment is essential to the experiment (e.g. due to sample instability in air or water), the ±35° series acquired

during temperature or gas treatment could be supplemented with a more detailed ±65° scan both before and after the experiment. In the latter case, the acquisition of supplementary angles before and after the experiment may supplement the deep learning method for allowing training of data reconstruction of the more limited angle scans. Improved data quality could also naturally be obtained by an increased number of projections, i.e. choosing a more appropriate level of angular sampling on the non-missing-wedge, which was undersampled in the present work. In any case, the extended time required for appropriate sampling over a suitable angular range should be carefully considered for potential *in situ* experiments, where PXCT series should be acquired during long sequences of different experimental conditions. Furthermore, while not optimal for technical catalysts where the sample is ideally studied with a minimum of preparation to preserve the structure and function, reducing the sample thickness may relax somewhat the angular requirements for tomographic reconstruction (Madejski *et al.*, 2018). In summary, this proof-of-concept acquisition of a missing wedge dataset complete with preliminary reconstruction indicates the potential of the 3G cell for collecting full 3D data series, although further development of acquisition parameters and reconstruction methods is certainly a priority. In future, by utilising the full function of the 3D cell, the ability to record even limited 3D data series under fully *in situ* conditions should prove to be interesting for the further development of synchrotron PXCT. The feasibility of such experiments is indicated here using the 3G cell apparatus.
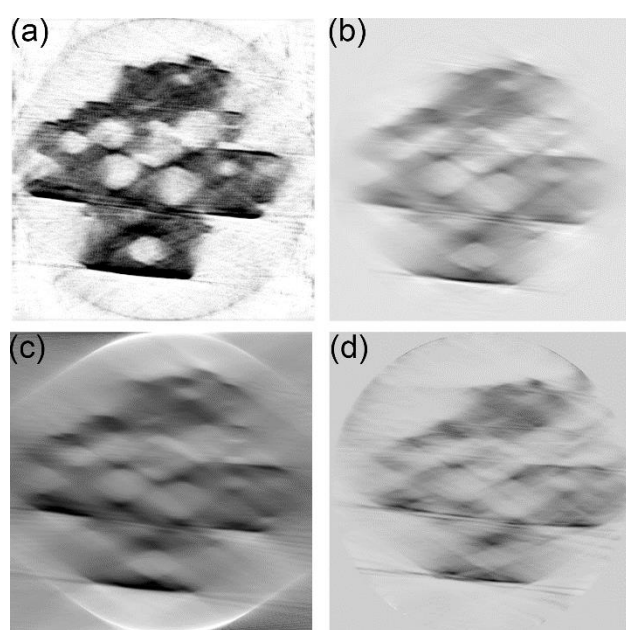
Figure 8 Single slice following tomographic reconstruction of the hierarchical zeolite sample from limited-angle data by: (a) an in-house deep learning method (under development at P06); (b) SART from the "scikit-image" Python package; (c) SIRT from the TomoJ plugin of FIJI software; (d) MLEM from the "TomoPy" Python toolbox.

4. Discussion

While the 2G and 3G cells described here have essentially finished commissioning and are ready to be employed for general users of beamline P06 and PETRA III, several improvements and future advances are nevertheless anticipated. Potential improvements to the cell design could focus on reducing the physical profile and mass even further, therefore leading to improved sample stability and minimizing the harmful effects of mechanical vibrations on spatial resolution. In any case sample stability has been shown to be marginally less crucial for ptychography than for analogous measurements using STXM for example, since ptychography can readily operate with a less focused beam or the sample out of the focal position, while still obtaining superior spatial resolution in the reconstructed data (Pfeiffer, 2017; Schroer *et al.*, 2017). For the 3G cell specifically, increasing the possible rotational angles by thinning the cell body design to increase the solid angle, or using alternative MEMS chips designed specifically for tomography may be readily achievable in the near future. To improve the range of experimental conditions, alternative window materials to thin Kapton could be explored to allow potential studies at elevated pressures greater than 100 kPa. Finally, there is significant room for development of 3D PXCT under *in situ* conditions, particularly concerning data analysis. It should be noted that reconstruction of 3D tomographic data with limited rotational angles may be challenging and prone to artefacts and errors depending on the reconstruction algorithm, although missing wedge measurements are typically acquired as standard using electron tomography. Data reconstruction could also be assisted by complementary TEM tomography, provided the sample dimensions allow for both TEM tomography and PXCT on the same region of interest. As the 2G and 3G cells are developed as an enabling technology for general users of beamline P06 and PETRA III, considering the range of potential users and sample types investigated at nanoprobe beamlines, it is feasible to assume that not all possible functionality of the cell may necessarily be needed simultaneously. In any case, the potential of the 3G cell for performing PXCT under *in situ* conditions, even with currently limited angular range, is a remarkable advance on currently available sample environments, and may find widespread use beyond the field of catalysis. Finally, it is also important to note the imminent arrival or planning of 4th generation and/or diffraction limited storage rings, such as ESRF-EBS, PETRA IV or SLS 2.0 (Schroer *et al.*, 2018). The improved beam properties are predicted to strongly benefit ptychography, particularly through the increased coherent flux available. The time is therefore right to develop and commission dedicated sample environments to take full advantage of improvements in imaging speed, spatial resolution and coherent flux, and to fully exploit these new capabilities for the catalysis and materials science community.

5. Conclusions

Two new modular 'nanoreactors' for complementary imaging at synchrotron radiation sources and in electron microscopes have been designed and commissioned at the hard X-ray nanoprobe endstation at beamline P06 of the PETRA III synchrotron radiation source. The cells offer numerous advantages over previously available sample environments. *In situ* XRP studies of thermal annealing processes under gas flow on monolithic np-Au were successfully conducted using an accurate and easily controlled heating and gas flow setup. For the implementation of thermal annealing processes, the sample deposition, accurate control and ease of use of the temperature controller setup are of high importance. Complementary TEM measurements on the same MEMS chip were also demonstrated, showing the ability to asses multiple hierarchical length scales of the same sample. Hierarchical zeolite samples were used to demonstrate the tilting capability of the cells for potential ptychographic tomographic studies on catalysts and functional materials either: (i) under *in situ* conditions, or (ii) through sequential treatment under reaction conditions, followed by imaging outside of the cell. However, the limitations of collecting and reconstructing tomography data with less than 180° angular range should be carefully considered. Other potential studies may include: (i) elemental analysis through fluorescence measurements at the synchrotron or using complementary TEM-EDX, (ii) crystallinity analysis through large angle XRD at the synchrotron and/or SAED for electron microscopy, (iii) oxidation state analysis through tuning incident X-ray energy around an absorption edge at the synchrotron (resonant ptychographic imaging), or by electron energy loss spectroscopy (EELS) for electron microscopy. A variety of applications ranging from gas sensing, gas storage, redox reactions, and thermal treatments, can benefit from use of these cells, which will presently be made available for general users of beamline P06 and PETRA III.

University Erlangen-Nuremberg) for preparation and provision of the zeolite sample; and finally Asst. Prof. Christian Damsgaard and Dr. Sina Baier (Technical University of Denmark) for discussions and preliminary work on designing the sample environment.

References

Andersen, A. H. & Kak, A. C. (1984). *Ultrasonic Imaging* **6**, 81-94.

Arslan, I., Tong, J. R. & Midgley, P. A. (2006). *Ultramicroscopy* **106**, 994-1000.

Bagge-Hansen, M., Wichmann, A., Wittstock, A., Lee, J. R. I., Ye, J., Willey, T. M., Kuntz, J. D., Van Buuren, T., Biener, J., Bäumer, M. & Biener, M. M. (2014). *J. Phys. Chem. C* **118**, 4078-4084.

Baier, S., Damsgaard, C. D., Klumpp, M., Reinhardt, J., Sheppard, T., Balogh, Z., Kasama, T., Benzi, F., Wagner, J. B., Schwieger, W., Schroer, C. G. & Grunwaldt, J.-D. (2017). *Microsc. Microanal.* **23**, 1-12.

Baier, S., Damsgaard, C. D., Scholz, M., Benzi, F., Rochet, A., Hoppe, R., Scherer, T., Shi, J., Wittstock, A., Weinhausen, B., Wagner, J. B., Schroer, C. G. & Grunwaldt, J. D. (2016). *Microsc. Microanal.* **22**, 178-188.

Baier, S., Wittstock, A., Damsgaard, C. D., Diaz, A., Reinhardt, J., Benzi, F., Shi, J. J., Scherer, T., Wang, D., Kubel, C., Schroer, C. G. & Grunwaldt, J. D. (2016). *RSC Adv.* **6**, 83031-83043.

Bañares, M. A. (2005). *Catal. Today* **100**, 71-77.

Beale, A. M., Jacques, S. D. M. & Weckhuysen, B. M. (2010). *Chem. Soc. Rev.* **39**, 4656-4672.

Bruyant, P. P. (2002). *J. Nucl. Med.* **43**, 1343-1358.

Buurmans, I. L. C. & Weckhuysen, B. M. (2012). *Nat. Chem.* **4**, 873-886.

da Silva, J. C., Pacureanu, A., Yang, Y., Bohic, S., Morawe, C., Barrett, R. & Cloetens, P. (2017). *Optica* **4**, 492-495.

da Silva, J. C., Mader, K., Holler, M., Haberthür, D., Diaz, A., Guizar-Sicairos, M., Cheng, W.-C., Shu, Y., Raabe, J., Menzel, A. & van Bokhoven, J. A. (2015). *ChemCatChem* **7**, 413-416.

De Smit, E., Swart, I., Creemer, J. F., Hoveling, G. H., Gilles, M. K., Tyliszczak, T., Kooyman, P. J., Zandbergen, H. W., Morin, C., Weckhuysen, B. M. & De Groot, F. M. F. (2008). *Nature* **456**, 222-225.

Diaz, A., Trtik, P., Guizar-Sicairos, M., Menzel, A., Thibault, P. & Bunk, O. (2012). *Phys. Rev. B* **85**, 1-4.

Dierolf, M., Menzel, A., Thibault, P., Schneider, P., Kewish, C. M., Wepf, R., Bunk, O. & Pfeiffer, F. (2010). *Nature* **467**, 436-439.

Fam, Y., Sheppard, T. L., Diaz, A., Scherer, T., Holler, M., Wang, W., Wang, D., Brenner, P., Wittstock, A. & Grunwaldt, J.-D. (2018). *ChemCatChem* **10**, 2858-2867.

Frenkel, A. I. & Van Bokhoven, J. A. (2014). *J. Synchrotron Radiat.* **21**, 1084-1089.

Gocyla, M., Kuehl, S., Shviro, M., Heyen, H., Selve, S., Dunin-Borkowski, R. E., Heggen, M. & Strasser, P. (2018). *ACS Nano* **12**, 5306-5311.

Grunwaldt, J. D. & Clausen, B. S. (2002). *Top. Catal.* **18**, 37-43.

Grunwaldt, J. D. & Schroer, C. G. (2010). *Chem. Soc. Rev.* **39**, 4741-4753.

Grunwaldt, J. D., Wagner, J. B. & Dunin-Borkowski, R. E. (2013). *ChemCatChem* **5**, 62-80.

Guizar-Sicairos, M., Diaz, A., Holler, M., Lucas, M. S., Menzel, A., Wepf, R. A. & Bunk, O. (2011). *Opt. Express* **19**, 21345-21357.

Guizar-Sicairos, M., Holler, M., Diaz, A., da Silva, J. C., Tsai, E. H. R., Bunk, O., Martinez-Perez, C., Donoghue, P. C. J., Wellman, C. H. & Menzel, A. (2015). *Proc. SPIE*, **9592**, 9592A.

Guizar-Sicairos, M., Thurman, S. T. & Fienup, J. R. (2008). *Opt. Lett.* **33**, 156-158.

Hönig, S., Hoppe, R., Patommel, J., Schropp, A., Stephan, S., Schöder, S., Burghammer, M. & Schroer, C. G. (2011). *Opt. Express* **19**, 16324-16329.

Hoppe, R., Reinhardt, J., Hofmann, G., Patommel, J., Grunwaldt, J. D., Damsgaard, C. D., Wellenreuther, G., Falkenberg, G. & Schroer, C. G. (2013). *Appl. Phys. Lett.* **102**, 203104.

Høydalsvik, K., Bø Fløystad, J., Zhao, T., Esmaeili, M., Diaz, A., Andreasen, J. W., Mathiesen, R. H., Rønning, M. & Breiby, D. W. (2014). *Appl. Phys. Lett.* **104**, 241909.

Huang, X., Conley, R., Bouet, N., Zhou, J., Macrander, A., Maser, J., Yan, H., Nazaretski, E., Lauer, K., Harder, R., Robinson, I. K., Kalbfleisch, S. & Chu, Y. S. (2015). *Opt. Express* **23**, 12496-12507.

Ihli, J., Diaz, A., Shu, Y., Guizar-Sicairos, M., Holler, M., Wakonig, K., Odstrcil, M., Li, T., Krumeich, F., Müller, E., Cheng, W.-C., van Bokhoven, J. A. & Menzel, A. (2018). *J. Phys. Chem. C* **122**, 22920-22929.

Ihli, J., Jacob, R. R., Holler, M., Guizar-Sicairos, M., Diaz, A., da Silva, J. C., Ferreira Sanchez, D., Krumeich, F., Grolimund, D., Taddei, M., Cheng, W. C., Shu, Y., Menzel, A. & van Bokhoven, J. A. (2017). *Nat. Commun.* **8**, 809.

Kupsch, A., Lange, A., Hentschel, M. P., Lueck, S., Schmidt, V., Grothausmann, R., Hilger, A. & Manke, I. (2016). *J. Microsc.* **261**, 36-45.

Lackmann, A., Bäumer, M., Wittstock, G. & Wittstock, A. (2018). *Nanoscale* **10**, 17166-17173.

Larsson, E., Gursoy, D., De Carlo, F., Lilleodden, E., Storm, M., Wilde, F., Hu, K., Muller, M. & Greving, I. (2019). *J. Synchrotron Radiat.* **26**, 194-204.

Li, T., Ihli, J., Ma, Z., Krumeich, F. & van Bokhoven, J. A. (2019). *J. Phys. Chem. C* **123**, 8793-8801.

Machoke, A. G., Beltrán, A. M., Inayat, A., Winter, B., Weissenberger, T., Kruse, N., Güttel, R., Spiecker, E. & Schwieger, W. (2015). *Adv. Mater.* **27**, 1066-1070.

Madejski, G., Lucas, K., Pascut, C. F., Webb, F. K. & McGrath, L. J. (2018). *Membranes* **8**.

Maiden, A. M. & Rodenburg, J. M. (2009). *Ultramicroscopy* **109**, 1256-1262.

Messaoudii, C., Boudier, T., Sanchez Sorzano, C. O. & Marco, S. (2007). *BMC Bioinformatics* **8**, 288-288.

Midgley, P. A. & Dunin-Borkowski, R. E. (2009). *Nat. Mater.* **8**, 271.

Odstrcil, M., Holler, M., Raabe, J. & Guizar-Sicairos, M. (2018). *Proc. SPIE* **10656**, 10656OU.

Patil, N., Skjønsfjell, E. T. B., Van den Brande, N., Chavez Panduro, E. A., Claessens, R., Guizar-Sicairos, M., Van Mele, B. & Breiby, D. W. (2016). *PLoS One* **11**, e0158345.

Pfeiffer, F. (2017). *Nat. Photonics* **12**, 9-17.

Piazza, V., Weinhausen, B., Diaz, A., Dammann, C., Maurer, C., Reynolds, M., Burghammer, M. & Köster, S. (2014). *ACS Nano* **8**, 12228-12237.

Przybilla, T., Zubiri, B. A., Beltrán, A. M., Butz, B., Machoke, A. G. F., Inayat, A., Distaso, M., Peukert, W., Schwieger, W. & Spiecker, E. (2018). *Small Methods* **2**, 1700276.

Ren, G. Q., Tang, Y., Liu, K. P., Su, Y., Miao, S., Liu, W., Cong, W. M., Wang, X. D., Li, W. Z., Li, J. & Zhang, T. (2018). *Nano. Lett.* **18**, 6489-6493.

Sala, S., Kuppili, V. S. C., Chalkidis, S., Batey, D. J., Shi, X., Rau, C. & Thibault, P. (2018). *J. Synchrotron Radiat.* **25**, 1214-1221.

Schindelin, J., Arganda-Carreras, I., Frise, E., Kaynig, V., Longair, M., Pietzsch, T., Preibisch, S., Rueden, C., Saalfeld, S., Schmid, B., Tinevez, J.-Y., White, D. J., Hartenstein, V., Eliceiri, K., Tomancak, P. & Cardona, A. (2012). *Nature Methods* **9**, 676.

Schroer, C. G., Agapov, I., Brefeld, W., Brinkmann, R., Chae, Y.-C., Chao, H.-C., Eriksson, M., Keil, J., Nuel Gavalda, X., Rohlsberger, R., Seeck, O. H., Sprung, M., Tischer, M., Wanzenberg, R. & Weckert, E. (2018). *J. Synchrotron Radiat.* **25**, 1277-1290.

Schroer, C. G., Seyrich, M., Kahnt, M., Botta, S., Döhrmann, R., Falkenberg, G., Garrevoet, J., Lyubomirskiy, M., Scholz, M., Schropp, A. & Wittwer, F. (2017). *Proc. SPIE* **10389**, 10389OE.

Schropp, A., Hoppe, R., Patommel, J., Samberg, D., Seiboth, F., Stephan, S., Wellenreuther, G., Falkenberg, G. & Schroer, C. G. (2012). *Appl. Phys. Lett.* **100**, 253112.

Schwieger, W., Machoke, A. G., Weissenberger, T., Inayat, A., Selvam, T., Klumpp, M. & Inayat, A. (2016). *Chem. Soc. Rev.* **45**, 3353-3376.

Seiboth, F., Schropp, A., Scholz, M., Wittwer, F., Rödel, C., Wünsche, M., Ullsperger, T., Nolte, S., Rahomäki, J., Parfeniukas, K., Giakoumidis, S., Vogt, U., Wagner, U., Rau, C., Boesenberg, U., Garrevoet, J., Falkenberg, G., Galtier, E. C., Ja Lee, H., Nagler, B. & Schroer, C. G. (2017). *Nat. Commun.* **8**, 14623.

Shapiro, D. A., Yu, Y. S., Tyliszczak, T., Cabana, J., Celestre, R., Chao, W., Kaznatcheev, K., Kilcoyne, A. L. D., Maia, F., Marchesini, S., Meng, Y. S., Warwick, T., Yang, L. L. & Padmore, H. A. (2014). *Nat. Photonics* **8**, 765-769.

Shi, J., Mahr, C., Murshed, M. M., Gesing, T. M., Rosenauer, A., Bäumer, M. & Wittstock, A. (2017). *Phys. Chem. Chem. Phys.* **19**, 8880-8888.

Shi, J., Mahr, C., Murshed, M. M., Zielasek, V., Rosenauer, A., Gesing, T. M., Bäumer, M. & Wittstock, A. (2016). *Catal. Sci. Technol.* **6**, 5311-5319.

Shi, J., Schaefer, A., Wichmann, A., Murshed, M. M., Gesing, T. M., Wittstock, A. & Bäumer, M. (2014). *J. Phys. Chem. C* **118**, 29270-29277.

Stierle, A., Keller, T. F., Noei, H., Vonk, V. & Roehlsberger, R. (2016). *Journal of Large-Scale Research Facilities* **2**, 1-9.

Thibault, P., Dierolf, M., Menzel, A., Bunk, O., David, C. & Pfeiffer, F. (2008). *Science* **321**, 379-382.

Thomas, J. M. & Hernandez-Garrido, J. C. (2009). *Angew. Chem. Int. Ed.* **48**, 3904-3907.

Topsøe, H. (2003). *J. Catal.* **216**, 155-164.

Van den Brande, N., Patil, N., Guizar-Sicairos, M., Claessens, R., Van Assche, G., Breiby, D. W. & Van Mele, B. (2017). *Org. Electron.* **41**, 319-326.

van der Walt, S., Schönberger, J. L., Nunez-Iglesias, J., Boulogne, F., Warner, J. D., Yager, N., Gouillart, E. & Yu, T. (2014). *PeerJ* **2**, e453.

Van Heel, M. & Schatz, M. (2005). *J. Struct. Biol.* **151**, 250-262.

van Ravenhorst, I. K., Vogt, C., Oosterbeek, H., Bossers, K. W., Moya-Cancino, J. G., van Bavel, A. P., van der Eerden, A. M. J., Vine, D., de Groot, F. M. F., Meirer, F. & Weckhuysen, B. M. (2018). *Angew. Chem. Int. Ed.* **57**, 11957-11962.

Van Riessen, A., Rickard, W. D. A., Williams, R. P. & Van Riessen, G. A. (2017). *J. Ceram. Sci. Technol.* **8**, 421-431.

Vila-Comamala, J., Diaz, A., Guizar-Sicairos, M., Mantion, A., Kewish, C. M., Menzel, A., Bunk, O. & David, C. (2011). *Opt. Express* **19**, 21333-21344.

Weckhuysen, B. M. (2002). *Chem. Commun.* **2**, 97-110.

Weckhuysen, B. M. (2009). *Angew. Chem., Int. Ed.* **48**, 4910-4943.

Weker, J. N., Huang, X. & Toney, M. F. (2016). *Curr. Opin. Chem. Eng.* **12**, 14-21.

Wichmann, A., Wittstock, A., Frank, K., Biener, M. M., Neumann, B., Mädler, L., Biener, J., Rosenauer, A. & Bäumer, M. (2013). *ChemCatChem* **5**, 2037-2043.

Wise, A. M., Weker, J. N., Kalirai, S., Farmand, M., Shapiro, D. A., Meirer, F. & Weckhuysen, B. M. (2016). *ACS Catal.* **6**, 2178-2181.

Yan, H., Conley, R., Bouet, N. & Chu, Y. S. (2014). *J. Phys. D* **47**, 263001.

Zečević, J., de Jong, K. P. & de Jongh, P. E. (2013). *Curr. Opin. Solid. St. M.* **17**, 115-125.

Zhu, C., Harder, R., Diaz, A., Komanicky, V., Barbour, A., Xu, R., Huang, X., Liu, Y., Pierce, M. S., Menzel, A. & You, H. (2015). *Appl. Phys. Lett.* **106**, 101604.

Supporting information

S1. Gas flow simulation of 2G/3G cells

In ANSYS AIM (Student Version, ANSYS, Inc.), Fluid Flow template module was used to simulate the gas flow in the 2G and 3G cell. Specific parameters were kept as default unless specifically mentioned. The geometry was generated by the integrated Space Claim Direct Modeler (SDCM) and "Define mesh manually" was chosen. In Fluid-specific options, "Swirling flow" was ticked to enable any significant rotating or twisting movement of the gas. The simulation focus was set as "Steady-state fluid flow". Number of fluid regions was selected to be "1", i.e. Air as the Material Sample, and "Compressible flow (ideal gas)" was ticked as an additional flow physics. For the meshing process settings, the resolution was set to 4, "Fluid flow or fluid-solid heat transfer" was selected for Engineering intent, and the refinement mechanism of "Curvature and proximity" was used. In Mesh controls, the element shape was set to "Automatic", where it meshed sweepable bodies with hexahedrons and provided a tetrahedral mesh on bodies that were not sweepable. The number of generated nodes was 46556 for 2G cell and 95272 for 3G cell, respectively.

For the Physics parameters, the whole SDCM-generated volume was specified as the location of Physics Regions. "Laminar" flow model was selected as the Flow Model since a Reynolds number (Re) of 9 was estimated according to: $Re = \frac{\rho * v * D_H}{\mu}$, where ρ is the mass density of air (1.1839 kg m^{-3} at T = 298 K), v is the mean velocity of air (0.236 m s^{-1} in this case from a volumetric flow of 1 ml min^{-1}), D_H is the hydraulic diameter of the inlet/outlet channel (0.3 mm), and μ is the dynamic viscosity of air (18.6 µPa s). The Inlet/Outlet Boundary was located on either one cross-section face of the long cylindrical channels with "Mixed" subsonic-supersonic regime and Gauge static pressure of 0 Pa. Additional parameter settings were for the inlet with gas Velocity magnitude of 0.236 m s^{-1} and Temperature of 298 K. The rest of the faces on the SDCM-generated volume was determined as the Wall Boundary. The Solver Options was left as default, where the solution would converge with Residual Tolerance of 1E-05 and Maximum iteration number of 1000; Solution advancement exponent was kept 0 under Calculation Control; and "Least squares cell-based" Gradient method was used for Discretization Control with "Second-order upwind" Advection and "Automatic" Pressure scheme. As the results, the convergence criteria were met after 45 iterations with residual tolerances up to 9.69E-06 for 2G cell, and 773 iterations with residual tolerances up to 2.15E-07 for 3G cell. The fluid flow profiles of the 2G and 3G cell are displayed in Figure 3 of the manuscript.

S2. Sample preparation of np-Au series via FIB

The description below (Figure S1-S4) only applies to the preparation of np-Au samples. Each original sample was a solid pellet, a piece of which was deposited on a SEM stub and then on a lift-out grid, which acted as an intermediate stage to the final sample holder, i.e. MEMS chip (Figure S1). All sample preparation steps were performed in a dual-beam focused ion beam. For details in each stage after mounting the stub, the piece was cut again and shaped into a smaller block / trapezoidal prism (Figure S2). The block was then transferred onto the lift-out grid, where a smaller wedge shape was eventually obtained (Figure S3). Last, the final transfer onto the MEMS-chip was made on the spiral center area of the chip and glued with Pt on the corner to stabilize the position (Figure S4).
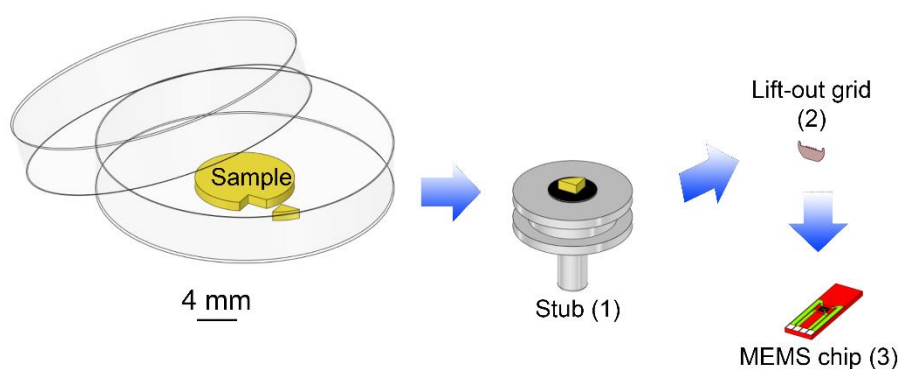
Figure S1 Overview of np-Au sample preparation on the MEMS chip via FIB.
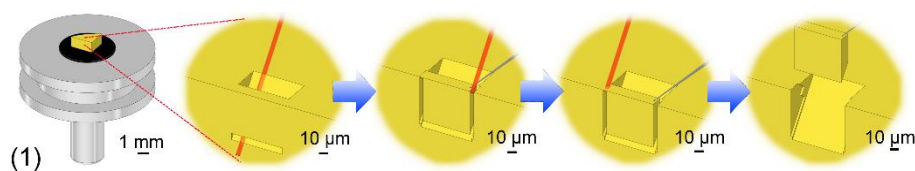
Figure S2 Initial np-Au extraction on a SEM stub to make a block for preparing several samples.
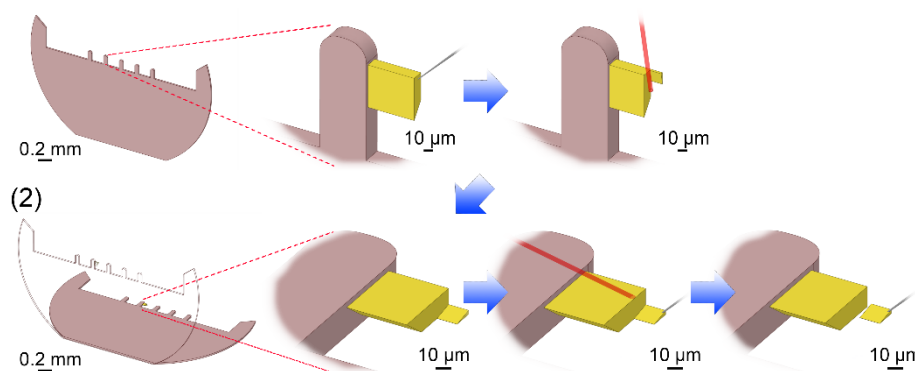
Figure S3 Final cut after transfer to intermediate lift-out grid and thinning of block into a wedge.

Figure S4 Transfer and deposition of the wedge on the MEMS chip.

S3. Temperature stability of the heating interface system

Since the MEMS chips and parts of heating interface system are commercially available and tested, the temperature readout and control process proved to be robust as shown in Figure S5. Excellent stability can be observed in the step functions between heating points, where fluctuations of <1 K were observed during temperature adjustment.
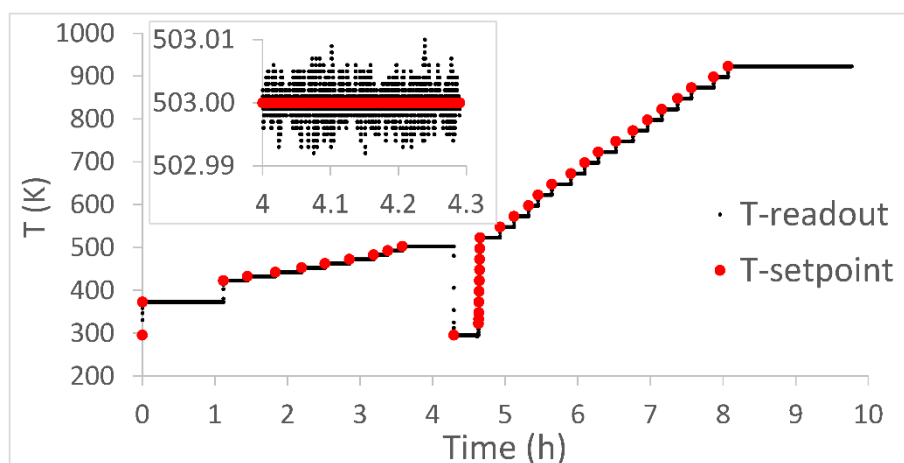

Figure S5 Plot of temperature readout vs time via the integrated temperature control system, recorded during thermal annealing study of nanoporous gold. The valley between the fourth and fifth hour of the measurement resulted from pausing the experiment due to loss of beam.

S4. Determination of the spatial resolution

To estimate the spatial resolution of the ptychograms obtained, a Fourier Ring Correlation (FRC) analysis was performed (Van Heel & Schatz, 2005), depicted in Figure S6 for colloidal Au, Figure S7 for nanoporous gold, and Figure S8 for the hierarchical zeolite particle. The intersection of the FRC datapoint with the 1 -bit threshold curve provides an estimation of the spatial resolution in nm averaged over the whole image and all directions.
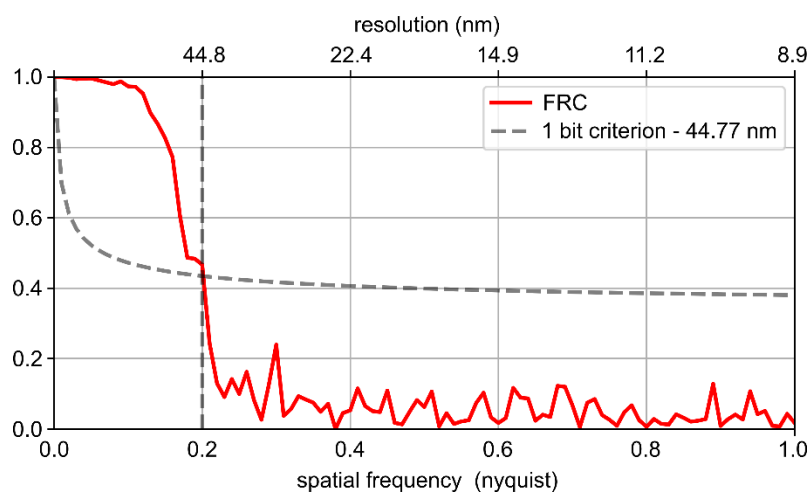
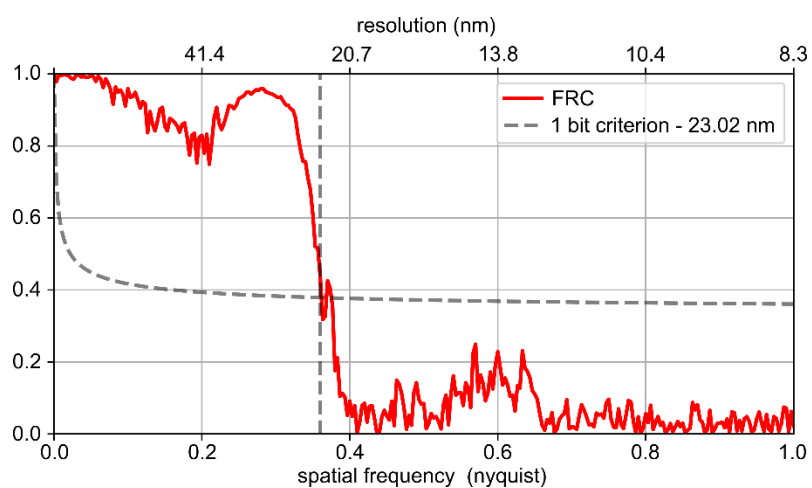**Figure S6** FRC of the ptychogram of colloidal Au nanoparticles.

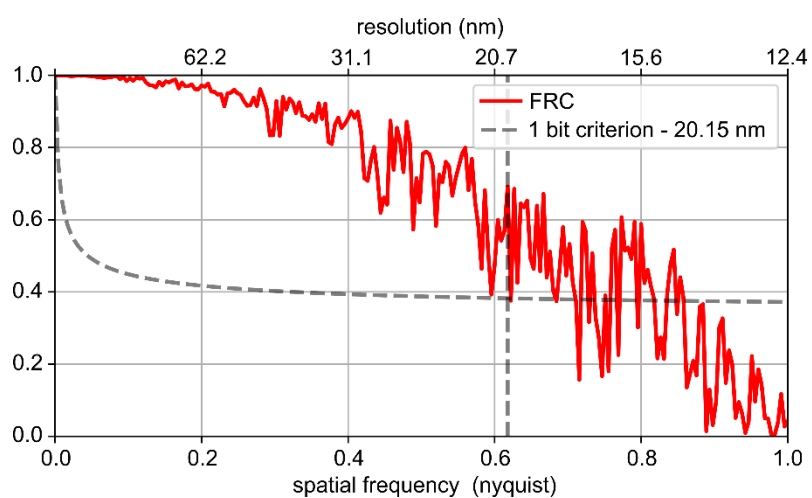**Figure S7** FRC of the ptychogram of np-Au sample.

Figure S8 FRC of the ptychogram of zeolite.

In addition to FRC, the resolution of the images was also estimated with a sharp edge fitting as shown in Figure S9. This was performed by drawing a line profile across a sharp contrast feature and counting the number of pixels through which the line passes. It should be noted that this method relies on the presence of sharp features, and is therefore dependent on the specific sample and image contrast. In general, lower estimations of resolution can be expected than for FRC. In particular, since the colloidal gold and zeolite could be clearly measured against the background, a sharper contrast gradient was observed. On the other hand, the np-Au sample is significantly thicker, while the void measured probably does not penetrate through the entire sample.
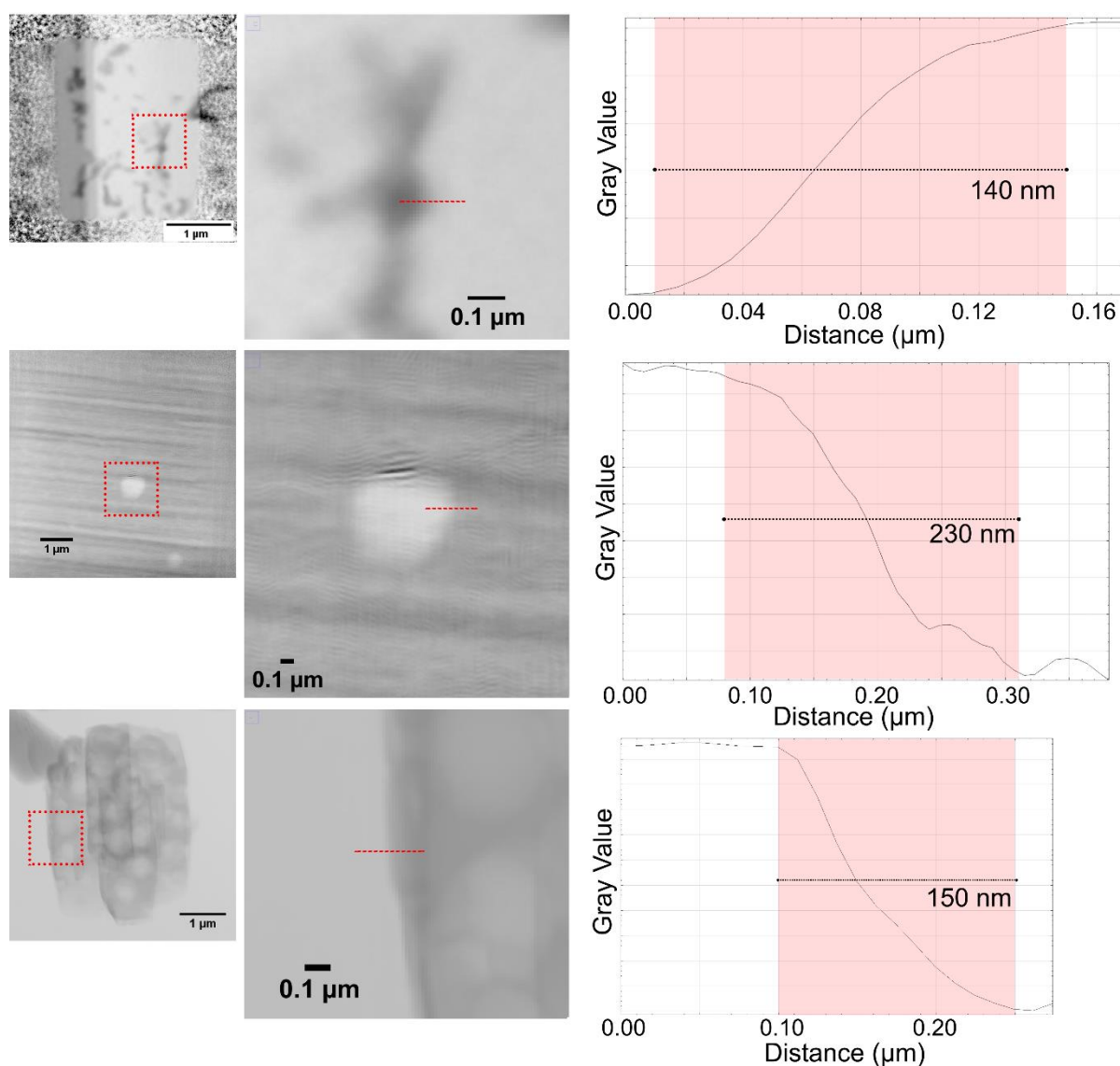

Figure S9   Estimation of spatial resolution via 'Edge Detection' method in FIJI software. The spatial resolution is indicated by intensity difference near the edge area highlighted in red from the graphs. Top: colloidal Au nanoparticles, middle: np-Au, bottom: hierarchical zeolite.

S5. *In situ* sintering of Au colloids – early cell prototypes using 2G cell

A solution of colloidal Au nanoparticles stabilized in citrate (Sigma-Aldrich Chemie GmbH, Taufkirchen, DE) with ~50 nm uniform particle size were applied directly to the sample area of the MEMS chips and the solvent left to evaporate for one hour under flowing air. The experiment using colloidal Au nanoparticle sample was performed at the nanofocus endstation of beamline P06 at the PETRA III synchrotron radiation source (Hamburg, Germany) (Schroer et al., 2017), using the energy of 15 keV, nano-focusing refractive X-ray lenses as the optics, and EIGER X 4M detector. The sample was positioned in the beam focus and located at 4.16 m from the detector. Moreover, the sample was scanned under 2-6 min per image with a field of view of 2.5 x 2.5 μm^2, exposure time of 50 ms, 500 scanpoints, and scanning step size of 100 nm. The algorithm used for ptychographic reconstruction was based on the (e)PIE algorithm. Cropping the diffraction patterns to 256×256 pixels led to a pixel size of 8.9 nm in the reconstructed images. To estimate the spatial resolution, a Fourier ring correlation (FRC) analysis was performed.

During measurement of the Au colloid sample, XRF signal was collected with a single channel Vortex silicon drift detector at 50 nm intervals with a collection time of 50 ms/pixel. The detector was placed on a moveable table and was located at an angle approximately 72 ° to the incident beam. It should be noted that the cell body blocks positioning of the detector ideally perpendicular to the incident beam. An XRF scan in high flux mode was recorded by scanning the sample over a field of view of 5x5 and 15×15 μm^2 with a step size of 50 nm. At each scanning position an XRF spectrum was collected for an exposure time of 2 s. The XRF spectra were fitted by AXIL software for the analysis of line intensities of the elements.

Colloidal Au particles with a size of 50 nm were utilized to confirm the applicability and feasibility of the 2G cell for *in situ* XRP and XRF. For this study, an early prototype of the 2G cell was used. This prototype consisted of the same physical cell profile shown in Figure 2 including electrical contacts, but without the gas tight O-ring and window assembly. Experiments were therefore performed only at elevated temperature up to 773 K but with ambient gas conditions. The ptychography images (Figure S10 – top row) imply that the spatial resolution should be at least 50 nm as colloidal Au can be clearly resolved, where high local concentration of colloidal Au is indicated by the darker intensity. Using FRC, the spatial resolution was in fact estimated to be 45 nm as shown in Figure S6. However, the Au fluorescence maps (Figure S10 – bottom row) are more suitable for locating colloidal Au, with increased local concentration leading to higher fluorescence counts. The Au colloids showed a distribution of larger connected ligaments, likely from clustered bunches of colloids, together with a homogeneous distribution of smaller particles, particularly visible in the upper middle of Figure S10a-b. During temperature treatment, the colloidal Au underwent several modifications including aggregation and/or recombination of individual particles into larger clusters. This was evidenced by the contraction of ligament shapes into spherical bodies which began already at 423 K, together with

the apparent disappearance of smaller particles in close vicinity to the more densely concentrated ones. These observations are typically expected for unsupported particles at elevated temperatures, at which the organic surfactant likely decomposes leading to aggregation. The complete disappearance of many smaller Au particles was also observed particularly at 773 K, which was somewhat unexpected since particle migration may not be expected to proceed across several microns. However, this could be due to the unstable deposition of unsupported particles directly on the Si_3N_4 window of the MEMS-chip, so the thermal effect may have caused them to significantly drift or fall away from the chip. As noted above, instead of the Digiheater temperature control unit, a variable voltage power supply and an IR thermographic camera were used as in previous work(Baier, Damsgaard, *et al.*, 2016). A typical IR thermography image captured from the cell during operation is shown in Figure S11. In this case, wires connected to the power supply were soldered directly to the power in/out contact of the printed circuit. As such, accurate control of the sample temperature was not guaranteed during the experiment. As noted previously, a sudden variation in local gas composition or local chemical reactions on the chip may cause significant temperature spikes, as observed in previous work(Baier, Damsgaard, *et al.*, 2016). This might also contribute to the sudden disappearance of colloidal Au at 773 K. This early case study highlights the necessity of a stable and dependable temperature control system, which was later integrated into both the 2G and 3G setups detailed in Figure 1 and Figure 2.
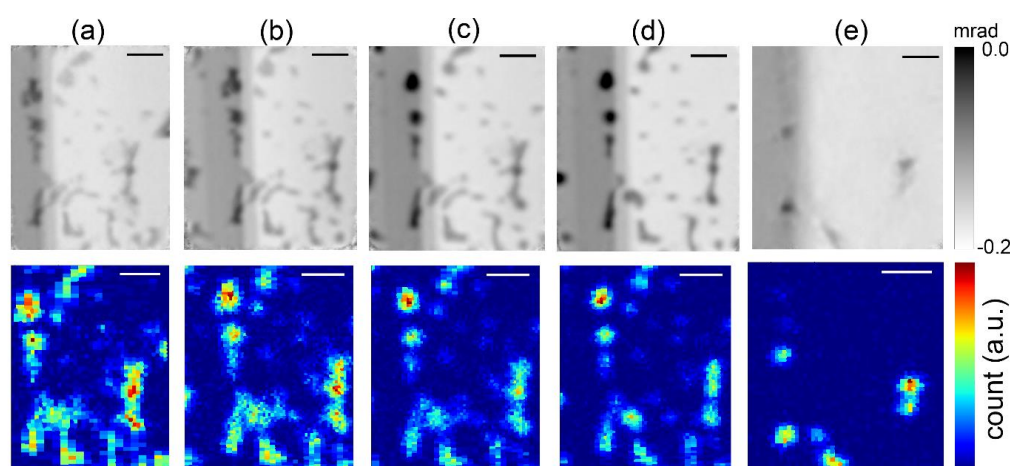

Figure S10 Ptychography images (top) and Au fluorescence maps (bottom) during thermal annealing of colloidal Au: (a) room temperature (293 K), (b) 423 K, (c) 573 K, (d) 723 K, and (e) 773 K. Dark spots in phase maps and high count zones in fluorescence maps indicate areas most rich in Au. Scale bars = 500 nm.
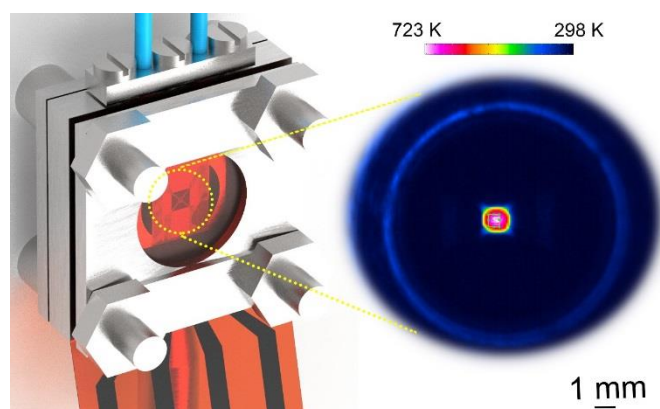
Figure S11 Depiction of the 2G cell (left) and the temperature profile on the MEMS chip recorded by IR thermography (right). The image was recorded inside the assembled prototype 2G cell during thermal annealing of the colloidal Au sample. Heating was performed via Joule heating principle on only 2 out of 4 pads located on MEMS chips, so the electrical currents could be converted into heat.

S6. Electron microscopy analysis of nanoporous gold

Additional high resolution TEM images, EDX analysis and selected area electron diffraction data were recorded on the nanoporous gold sample described in the study. Data was recorded on the sample deposited on a MEMS chip and placed within a Wildfire sample holder (DENSsolutions, Delft, NL), on a Titan 80-300 (FEI) microscope operated at an acceleration voltage of 300 kV in STEM and TEM mode, at the Institute of Nanotechnology (INT) at Karlsruhe Institute of Technology.
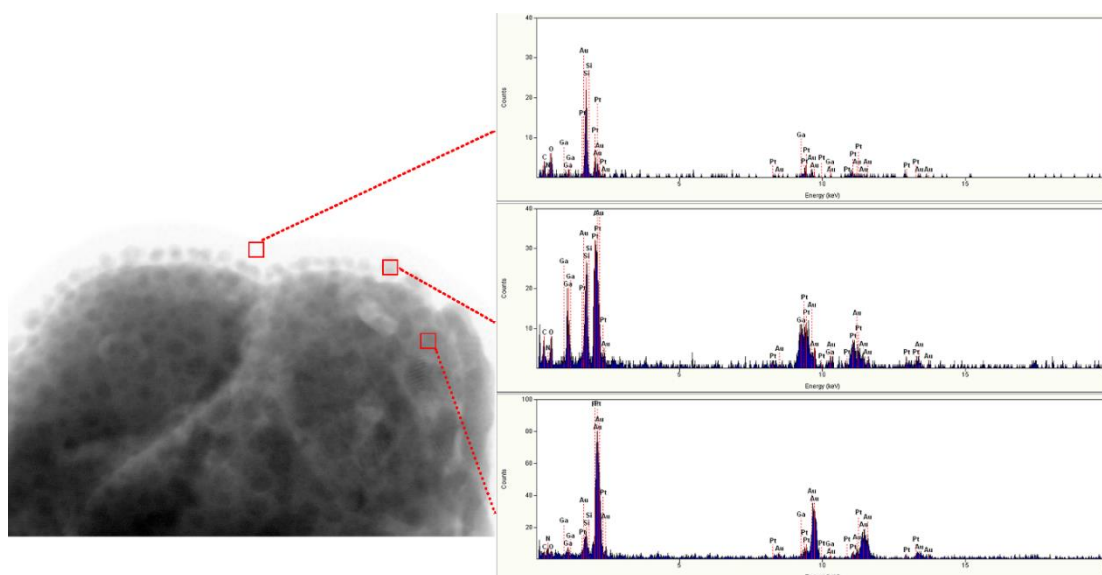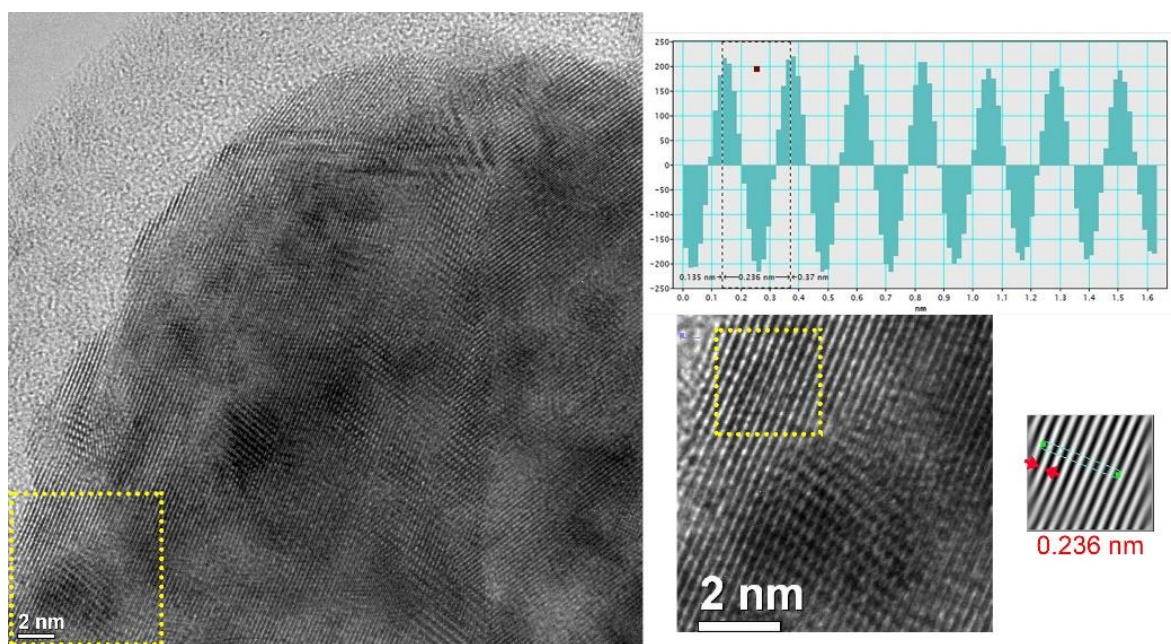

Figure S12 TEM-EDX data recorded on the nanoporous gold sample used for *in situ* ptychography. Analysis shows the presence of minor Si and Pt contaminants close to the Au ligament edges.

Table S1   Quantification of EDX spectra in Figure S12.

Element	Atomic %		
	Area 1	Area 2	Area 3
C	6.2	29.6	29.1
N	6.9	0.0	3.9
O	5.2	13.1	14.2
Si	21.3	32.0	52.7
Ga	0.1	12.1	0.0
Pt	0.0	10.6	0.0
Au	60.2	2.6	0.0

Figure S13 Lattice spacing measurement of fresh np-Au sample (highlighted area) via bright-field high resolution TEM, indicating d = 0.236 nm, belonging to (1 1 1) plane of Au metal (PDF 99-0056).
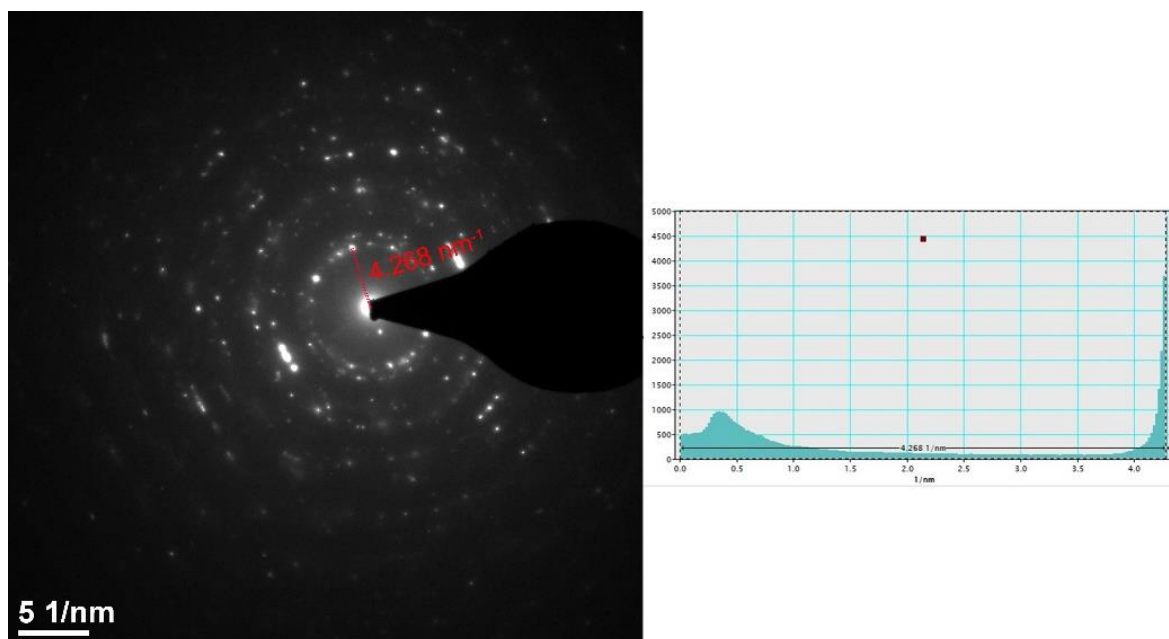
Figure S14 Lattice spacing measurement of fresh np-Au sample (between indicated points) via selected area electron diffraction, indicating d = 0.234 nm, belonging to (1 1 1) plane of Au metal (PDF 99-0056).